JOURNAL OF GEOPHYSICAL RESEARCH, VOL. 95, NO. B10, PAGES 15,779–15,803, SEPTEMBER 10, 1990

Origin of Mantle Peridotite: Constraints From Melting Experiments to 16.5 GPa

CLAUDE HERZBERG

Department of Geological Sciences, Rutgers University, New Brunswick, New Jersey

TIBOR GASPARIK

Mineral Physics Institute, Department of Earth and Space Sciences State University of New York, Stony Brook

HIROSHI SAWAMOTO

Department of Earth Sciences, Nagoya University, Chikusa, Nagoya, Japan

Experimental data are reported for the melting of komatiite, peridotite, and chondrite compositions in the pressure range 5–16.5 GPa. All experiments were run using the multiple-anvil apparatus facilities at Nagoya and Stony Brook. Equilibrium between coexisting crystals and liquid is demonstrated to occur in less than 3 min in the 2100°C range. The anhydrous solidus in CaO-MgO-Al_2O_3-SiO_2 has been calibrated and is shown to be about 100° higher than that for naturally occurring peridotite (KLB1). All melting curves have positive dT/dP. The effect of pressure is to expand the crystallization field of garnet at the expense of all other phases, resulting in a change in the liquidus phase from olivine to garnet at high pressures. The melting of rocks which contain the four crystalline phases olivine, orthopyroxene, clinopyroxene, and garnet is restricted to enstatite-rich compositions such as chondrite. For these it is demonstrated that melting is peritectic, rather than eutectic, and takes the form L + Opx = Ol + Cpx + Gt. Partial melting yields liquids with the following properties: 5 GPa for komatiite; and 10–15 GPa for liquid peridotite with about 40% MgO, but one that is unlike mantle peridotite in that it is distinctly enriched in silica. These results provide a test and refutation of the model that upper mantle peridotite originated by direct initial melting of a chondritic mantle (Herzberg and O'Hara, 1985). Unlike chondrite, partial melting of peridotite does not usually involve orthopyroxene. Instead, it occurs by the generation of ultrabasic liquids along a cotectic involving L + Ol + Cpx + Gt. Although the thermal and compositional characteristics of this cotectic have not been fully calibrated, it is very likely that it will degenerate into a thermal minimum (L + Ol + Cpx + Gt), compositionally similar to komatiite at 5 GPa and mantle peridotite at 10–15 GPa. Peridotite liquids that occupy a thermal minimum can be derived from those formed from the melting of chondrite by removal of orthopyroxene, followed by fractional crystallization of olivine, clinopyroxene, and garnet. The possibility exists that the thermal minimum is compositionally identical to mantle peridotite in the 10–15 GPa range. If this can be confirmed by experiment, the upper mantle can be understood as having originated by the fractional crystallization of peridotite liquids in a large-scale differentiation event, consistent with magma ocean models for an early Earth.

1. INTRODUCTION

The development of the multiple-anvil apparatus has extended the limits of experimental igneous petrology from about 4 to 25 GPa (40–250 kbar [*Ohtani et al.*, 1986; *Ohtani and Sawamoto*, 1987; *Takahashi*, 1986; *Takahashi and Scarfe*, 1985; *Scarfe and Takahashi*, 1986; *Ito and Takahashi*, 1987; *Kato and Kumazawa*, 1986]). One of the most important results has been the discovery that basalts and picrites are restricted to partial melting processes at relatively low pressures, the 1- to 3-GPa range [*O'Hara*, 1968; *Kushiro*, 1973; *Green et al.*, 1979; *Fujii and Scarfe*, 1985; *Elthon and Scarfe*, 1984; *Presnall et al.*, 1979; *Stolper*, 1980]. At higher pressures, partial melts become increasingly enriched in MgO [*O'Hara et al.*, 1975] and range from komatiite to liquid peridotite [*Herzberg*, 1983; *Herzberg and O'Hara*, 1985; *Takahashi and Scarfe*, 1985; *Takahashi*, 1986; *Herzberg and Ohtani*, 1988]. Partial melting in the deep interior is characteristically ultrabasic, at least for volatile-free compositions, and basaltic volcanism is a surficial phenomenon.

The precise determination of liquid compositions that are stable on the anhydrous solidus at high pressures is essential for the testing and construction of hypotheses on the origin of ultrabasic rocks such as komatiites and peridotites. However, discriminating subtle but important differences among a range of possible magnesian compositions is a difficult problem because suitable glasses cannot be quenched for analysis by electron microprobe. Rather, all highly magnesian liquids solidify to a mat of quench crystals which require broad-beam analytical techniques. Such data can be obtained [*Ohtani et al.*, 1986; *Kato et al.*, 1988*a*] but are restricted to regions of the experimental charge where the area of quench liquid contains widely dispersed crystals, the area at and near the liquidus. Quench crystals formed at the solidus coexist with a high density of primary crystals, and the area available for analysis is typically less than the area of a broad electron microbeam.

Another method for determining the composition of liq-

Paper number 90JB00305.
0148-0227/90/90JB-00305$05.00

TABLE 1. Compositions of Starting Materials

	Komatiite (K)		Peridotite (P)		Chondrite (C)			
	Mix	DCP*	Mix	DCP*	Mix	DCP*	KLB1†	KLB1, DCP‡
SiO_2	47.00	46.38	46.50	47.16	50.25	50.20	44.48	44.30
TiO_2		...	...	...	...	...	0.16	0.12
Al_2O_3	9.90	10.98	6.10	6.36	5.06	5.15	3.59	3.54
FeO	...	...	...	...	...	...	8.10	8.59
MnO	...	...	...	...	...	...	0.12	0.14
MgO	34.00	33.39	42.00	41.93	40.88	40.14	39.22	39.50
CaO	9.10	8.99	5.40	5.59	3.81	3.91	3.44	3.03
Na_2O	...	...	...	...	...	...	0.30	0.30
K_2O	...	...	...	...	...	...	0.02	0.01
Cr_2O_3	...	...	...	...	...	...	0.31	...
NiO	...	...	...	...	...	...	0.25	...

Mix refers to the weighted oxide mix. DCP is direct current plasma emission spectroscopy.
*Analyzed by P. Milionis.
†From *Takahashi* [1986].
‡Analyzed by M. J. Carr.

uids on an ultrahigh-pressure solidus is the so-called shotgun technique. With this method, experiments are made on a selected number of starting material compositions, and the solidus melt at a pressure of interest is bounded by the nature of the liquidus phase for each composition. This method was extensively used for basaltic systems before the electron microprobe analysis of glasses rendered it obsolete. However, the shotgun technique remains the least ambiguous method available for melting experiments on ultrabasic compositions such as komatiite and liquid peridotites that cannot be quenched to glass.

In this paper, phase equilibria data are reported from melting experiments that have been run on a komatiite, two peridotites, and a chondrite composition. The pressures range from about 5 to 16.5 GPa (50–165 kbar). It is demonstrated that highly magnesian liquids are indeed generated on the solidus, but their compositions can depend on the form of the melting relations and on whether the liquids undergo fractional crystallization at depth. Specifically, melting at high pressures occurs at peritectic points or near thermal minima, rather than at eutectics, and the initial melts generated can evolve to different compositions by fractional crystallization.

Knowledge of the absolute temperatures for the anhydrous mantle solidus to pressures in the 100-kbar range has many important geophysical as well as petrological applications. The temperatures are essential in any quantitative model of the early melting and differentiation history of the Earth and are tied to such properties as the homologous temperature, viscosity, strain rates, and diffusion coefficients. Accordingly, an experimental method was developed in order to provide truly anhydrous data, yielding accurate melting temperatures to 16.5 GPa.

All experiments were run using the multiple-anvil press laboratories located at Nagoya University in Japan and the State University of New York (Stony Brook) in the United States. A great deal of effort was directed at developing an experimental method that permits phase equilibrium data to be obtained with a confidence level similar to that obtained with the piston-cylinder apparatus. The chief difficulties have arisen from large temperature gradients in the sample, short run times, and sample contamination due to container problems. We have explored these problems and conclude that experimental data reported by all investigators since the pioneering articles by *Takahashi* [1986] and *Ohtani et al.* [1986] are equilibrium results, permitting accurate petrogenetic conclusions to be drawn on the origin of many ultrabasic rocks.

2. Experimental Method

2.1. *Starting Materials*

Komatiite, peridotite, and chondrite analogue compositions in the system CaO-MgO-Al_2O_3-SiO_2 are reported in Table 1. The samples were prepared by mixing together oxide and carbonate reagents and sintering at 1200°C for 5 days. The resulting fine-grained mixtures contained forsterite, pyroxenes, anorthite, and unreacted oxides having the compositions shown in Table 1. Chemical analysis was done by direct current plasma emission spectrometry (DCP), accurate to ±2% relative [*Feigenson and Carr*, 1985].

A third composition consisted of spinel peridotite KLB1, kindly donated by E. Takahashi. The purpose of doing experiments on this composition was to compare for internal consistency the results reported by *Takahashi* [1986] and to calibrate the effects of other components such as FeO on lowering melting temperatures.

2.2. *High-Pressure Apparatus*

All experiments were done using an MA8-type configuration driven by guide blocks in the 2000-t presses located at Nagoya and Stony Brook. Both systems are very similar in that a uniaxial load is transmitted to the sample via a set of eight tungsten carbide anvils. Each cube has a corner truncated into a triangular face, and this creates an octahedral cavity within which the pressure assembly is contained (Figure 1). The essential differences between the two laboratories is in the design of the guide blocks, and these have been described in detail by *Ohtani* [1979] and *Gasparik* [1989].

2.3. *High-Pressure Assemblies*

Three different generations of assemblies where used, and these are shown in Figures 1*a*, 1*b*, and 1*c* in chronological

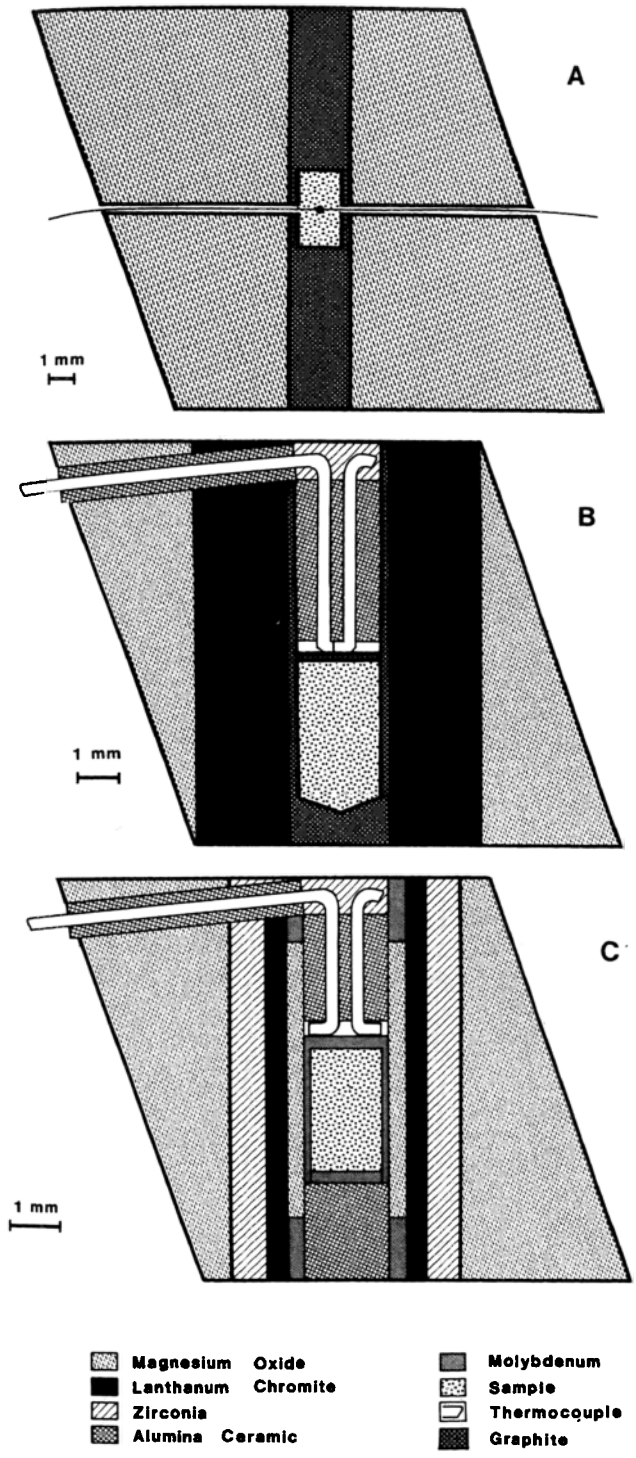

Fig. 1. High-pressure cell assemblies.

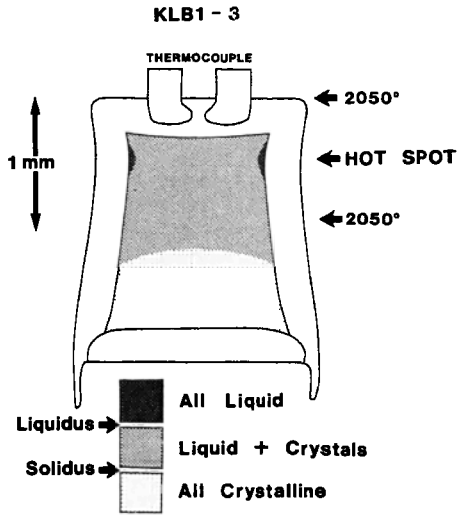

Fig. 2. Experimental result on KLB1 at 14 GPa.

order of development. Each is a section through an MgO octahedron containing the sample, resistance heater, thermocouple, and spacers.

Assembly A in Figure 1*a* was used at Nagoya University. It is an octahedron with an 18-mm edge length used with tungsten carbide anvils having a 12-mm corner truncation edge. This was used for experiments at pressures less than about 8 GPa with graphite as the heater. The design is similar to those used by *Takahashi* [1986] and *Ohtani and Kumazawa* [1981] in that the thermocouple enters through the sides of the heater, rather than down the axis (Figures 1*b* and 1*c*).

A disadvantage with this system is that a hole must be drilled in the heater in order to insert the thermocouple, and this creates local irregularities in resistivity and temperature. During a run the thermocouple can come in contact with the heater even for well-insulated assemblies; for example, this can arise from the reaction of lanthanum chromite with alumina thermocouple insultors. When this occurs, it gives rise to an ambiguity in temperature measurement because it is not clear where in the sample the nominal temperature is actually valid (see below).

Assembly B is the prototype axial thermocouple design used and developed at Nagoya University and patterned after standard piston-cylinder assemblies. Assembly B1 has an octahedral edge length of 14 mm, and B2 has an edge length of 18 mm. In both cases the thermocouple was configured down the axis of the heater, which is graphite for the 18-mm assembly and graphite and lanthanum chromite for the 14-mm assembly (Figure 1*b*). The thermocouple junction is unambiguously located, and the emf generated there is valid even if it comes in contact with the heater. Additionally, the thermocouple junction is located exactly in the middle of the assembly at the hot spot.

Assembly C is now the standard at Stony Brook and is similar to assembly B but has molybdenum or rhenium as the sample container. During the course of the experiment the thermocouple wires become embedded in the container (Figure 2), and the thermocouple ceramic/molybdenum contact becomes the effective thermocouple junction. This junction is not located in the hot spot as with assembly B, but instead, it is located slightly to one side of it (see below). Thermocouples used in all assemblies were W3% Re versus W25% Re.

2.4. *Temperature Measurement and Gradient*

Figure 2 is a map of the liquidus and solidus locations for experiment KLB1-3 (Table 2), and Figure 3 shows the sweeping of these isothermal surfaces across the sample with temperature increments of about 30°C. For accurate temperature measurement the location of the hot spot must

TABLE 2. Experimental Results

Run	T, °C	P,* GPa	P,† GPa	Time, min	Assembly	$T > Tc$	Tc	$T < Tc$
K-04	2015	8	7.5	1.0	A	L	L	L + Gt
								L + Gt + Ol
K-05	1720	5.3	5.1	0.5	A	L + Ol + Gt	all solid	all solid
K-06	1800	5.3	5.1	1.0	A		L + Ol	L + Ol + Gt
K-07	1835	8	7.5	0.2	A	all solid	all solid	all solid
K-08	1740	5.3	5.1	1.0	A	L + Ol + Gt	all solid	all solid
K-09	1790	8	7.5	1.0	A	all solid	all solid	all solid
K-10	2080	13	11.6	1.0	B1	L + Gt ?	all solid ?	all solid
						L + Gt + Ol ?		
K-11	2160	8	7.5	0.2	B2	L	L	L + Gt
K-12	1990	8	7.5	1.0	B2	L	L + Gt	L + Gt + Ol + Cpx
K-14	1750	6.6	6.3	0.2	B2	all solid	all solid	all solid
K-15	1860	6.6	6.3	1.0	B2	L	L + Gt + Ol	L + Gt + Ol + Cpx
						L + Gt		Gt + Ol + Cpx
K-16	1910	8	7.5	0.2	B2	all solid	all solid	all solid
K-17	1800	5.3	5.1	0.6	B2	L + Ol	L + Ol	L + Ol + Gt
K-18	1810	6.6	6.3	1.0	B2	all solid	all solid	all solid
P-01	1960	13	11.6	0.2	B1	all solid	all solid	all solid
P-02	2080	13	11.6	0.6	B1	L + Ol + Gt + Cpx	all solid	all solid
P-03	1970	10	9.2	0.2	B1	all solid	all solid	all solid
P-04	2100	10	9.2	1.0	B1	L	L	L + Ol
P-05	1970	5.3	5.1	4.0	B2	L	L	L + Ol
P-06	2220	13	11.6	1.0	B1	L	L	L + Ol
P-07	1870	5.3	5.1	1.0	B2	L + Ol	L + Ol	L + Ol + Gt
								L + Ol + Gt + Opx
								L + Ol + Gt + Cpx
								Ol + Gt + Cpx
P-08	2340	13	11.6	1.0	B1	L	L	
P-09	2050	10	9.2	0.2	B2	L + Ol	L + Ol	
P-10	2060	17.7	15.3	0.2	C	L + Gt	all solid	all solid
						L + Gt + Ol		
P-11	2185	17.7	15.3	0.2	C	L + Gt	L + Gt	L + Gt + Ol
								Gt + Ol
P-12	2185	16.0	14.0	2.5	C	L	L + Gt	L + Gt + Ol
								Gt + Ol
P-13	2055	16.0	14.0	3.0	C	all solid	all solid	all solid
P-14	2120	16.0	14.0	2.5	C	L + Gt	all solid	all solid
						L + Gt + Ol		
P-15	2185	16.0	14.0	3.0	C	L	L + Gt	L + Gt + Ol
								Gt + Ol
P-16	2080	11.0	10.0	4.0	C	L	L + Ol	L + Ol + Gt
								L + Ol + Gt + Cpx
								Ol + Gt + Cpx
P-17	2110	12.2	11.0	3.0	C	L	L	L + Ol
								L + Ol + Gt
								L + Ol + Gt + Cpx
								Ol + Gt + Cpx
C-2	2240	12.5	11.3	3.0	C	L	L	L + Gt
								L + Gt + Ol
C-3	2350	20.0	16.5	6.0	C		L + Gt	L + Gt + AnhB
								L + Gt + Sp
								Gt + Sp
C-4	2000	8.5	8.0	4.0	C	L	L + Ol	L + Ol + Gt
								L + Ol + Gt + Opx
								L + Ol + Gt + Opx + Cpx
								Ol + Gt + Opx + Cpx
C-5	2080	11.0	10.0	5.0	C	L	L + Ol + Gt	L + Ol + Gt + Opx
								L + Ol + Gt + Opx + Cpx
								Ol + Gt + Opx + Cpx
C-6	2150	12.5	12.0	4.0	C	L + Gt	L + Gt + Ol	L + Gt + Ol + Opx
								L + Gt + Ol + Opx + Cpx
								Gt + Ol + Cpx
C-7	2200	16.0	14.0	4.0	C	L	L + Gt	L + Gt + Ol
								L + Gt + Ol + Cpx
								Gt + Ol + Cpx
$C_{50}P_{50}$	2055	11.0	10.0	0.2	C	L	L + Ol	L + Ol + Gt
								L + Ol + Gt + Opx
								L + Ol + Gt + Opx + Cpx
$C_{25}P_{75}$	2080	11.0	10.0	5.0	C	L	L + Ol	L + Ol + Gt
								L + Ol + Gt + Cpx
								Ol + Gt + Cpx

TABLE 2. (continued)

Run	T, °C	P,* GPa	P,† GPa	Time, min	Assembly	T > Tc	Tc	T < Tc
KLB-1‡	2020	16.0	14.0	2.0	C			
KLB1-2	2020	16.0	14.0	8.0	C	all solid	all solid	all solid
KLB1-3	2050	16.0	14.0	6.0	C	L + Gt	L + Gt + Ol	L + Gt + Ol + Cpx Gt + Ol + Cpx
KLB1-4	2115	16.0	14.0	2.0	C	L L + Gt	L + Gt + Ol	
KLB1-5	2080	16.0	14.0	2.0	C	L L + Gt	L + Gt + Ol	
KLB1-6	2155	16.0	14.0	1.0	C	L	L	L + Gt L + Gt + Ol

All experiments on KLB1 contain also Mo-Fe alloy droplets. Abbreviations are defined as follows: L, liquid (quench crystals); Ol olivine; Gt, garnet; Cpx, clinopyroxene; Opx, orthopyroxene; Sp, modified spinel Mg_2SiO_4; and AnhB, phase anhydrous B.

*Pressure calibrations at room temperatue.

†Pressure calibrations at high temperature.

‡For run KLB1-1 there was pervasive melting, and H_2O was inadvertently introduced. Characteristics of $T > Tc$, Tc, and $T < Tc$ are not known.

be determined relative to the thermocouple junction. It is usually located exactly in the center of the assembly and can be identified in thin section using the following criteria: (1) in melting experiments the silicate liquid digests the molybdenum container preferentially at the hot spot; (2) the inner diameter of the molybdenum container is minimal at the hot spot; and (3) the white MgO sleeve that separates the molybdenum container from the lanthanum chromite heater (Figure 1*c*) is discolored brown nearest the hot spot. Using a micrometer eyepiece, the distance from the thermocouple junction to the hot spot is easily measured and is usually not greater than about 0.8 mm. Assuming a symmetrical distribution of temperature about the hot spot, the temperature can be assigned to an exact location in the charge (Figure 2). We have evidence, however, that the temperature gradient is actually somewhat asymmetrical, being steeper toward the thermocouple. This will yield nominal temperatures of melting that are somewhat too low.

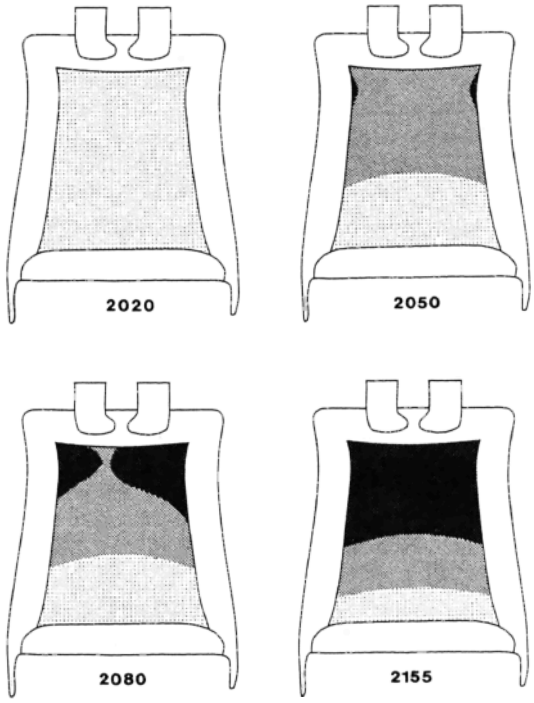

Fig. 3. Experimental results on KLB1 at 14 GPa and the temperatures shown (degrees Celsius).

By positioning the shifts in the solidus for KLB1 with increasing temperature (Figure 3), the temperature gradient has been determined to be about 50°C within 0.7 mm of the hot spot, steepening considerably beyond that. This is in excellent agreement with observations of the solidus shift made by *Takahashi* [1986]. It is also in excellent agreement with the temperature gradient measured directly by multiple thermocouples [*Gasparik*, 1989] and deduced from the solubility of enstatite in diopside [*Gasparik*, 1989; *Takahashi et al.*, 1982]. The relatively flat temperature distribution near the hot spot arises because lanthanum chromite is a semiconductor having a resistivity that decreases with increasing temperature [see *Takahashi*, 1986, Figure 4].

The flat temperature gradient associated with lanthanum chromite heaters is an experimental asset rather than a liability because two kinds of information can be simultaneously obtained from a single experiment. These are (1) phase stability at the temperature of the thermocouple junction and (2) portions of an isobaric phase diagram. For the latter a complete crystallization sequence can often be observed from the liquidus to the solidus in a single thin section, information that is exploited in the tabulation of experimental results (Table 2).

In addition to the axial temperature gradient, there exists a lateral temperature gradient, with temperatures increasing from the center of the sample to the sample/heater contact. This causes the isothermal liquidus and solidus surfaces to be convex in Figures 2 and 3. On the basis of Figure 3 we expect it to be about 30°C from the center to the edge. However, in many experiments we see evidence that it steepens even more near the sample/heater contact. This creates an important ambiguity in temperature measurement for assembly A if the thermocouple should come in contact with the heater. We have noted, for example, that an experiment containing L + Ol will typically have a small area of total liquid (L) at the sample/heater contact nearest the hot spot. The phase assemblage identified with the axial thermocouple configuration (assembly B; K-17) is L + Ol, whereas assembly A will erroneously read this as L (K-06). Side-entering thermocouple configurations are likely to cre-

ate locally high resistivities in the heater at the point of entry and locally high temperatures that do not correspond to those read by the thermocouple. Therefore phase assemblages in Table 2 reported for assembly A are valid in the center of the charge, rather than at the sample/heater contact. In general, a thermocouple entering through the side of an assembly will read melting temperatures that are too low (see also *Wei et al.* [this issue]).

A potential problem with the temperature gradient concerns the Soret diffusion of liquid components along it, as has been observed in experiments of lengthy duration [*Walker and DeLong*, 1982]. Should this occur, the control of composition on the phase equilibria would be lost, and the experimental observations would be rendered ambiguous. In order to test this problem the composition of the all-melt region above the liquidus in two experiments was determined. For a komatiite experiment (K-12), portions of the all-melt region quenched to a glass identical in composition to the starting material. For a peridotite experiment (P-12) the all-melt portion quenched to a mat of rapidly cooled "quench" crystals; unfocused electron microprobe analyses showed a wide range of values but no systematic variations in average values for the major elements along the temperature gradient. These results demonstrate that Soret diffusion did not occur during the 3-min duration of the experiments. The same result was reported by *Kato et al* [1988*b*].

In experiments of short duration, that is, less than about 3 min, portions of an isobaric phase diagram are preserved, with clearly identifiable primary crystals coexisting with intercumulus liquid (quench crystals; Figures 9 and 10). However, in experiments of longer duration the intercumulus melt is expelled toward the hot spot, and grain coarsening occurs in the minerals at the cold end (Figures 7 and 19). Similar observations have been made in low-pressure experiments [*Lesher and Walker*, 1988] where the transport fate of coexisting crystals and liquid was monitored in a thermal gradient. This process, called saturation gradient chemical diffusion [*Lesher and Walker*, 1988], occurs by diffusion of components in the liquid phase and may be an important way of making adcumulus igneous rocks [*Lesher and Walker*, 1988]. It is not clear, however, how nearly monomineralic layers seen in experimental charges will affect conclusions drawn about the equilibrium isobaric crystallization sequence. *Lesher and Walker* [1988] have suggested from theoretical grounds that this process should not create ambiguous interpretations of the liquidus phase; however, it will affect the modal proportions of crystalline phases that coexist along a cotectic equilibrium. We agree, because we have observed no peculiar changes in the nature of the liquidus phase as a function of time in any of our experiments.

2.5. *Pressure Generation and Measurement*

Pressures were calibrated by determining the uniaxial load required to produce a number of well-calibrated transitions, and the method has been described in numerous papers [*Ohtani*, 1979; *Takahashi*, 1986]. The Stony Brook calibration was reported elsewhere [*Gasparik*, 1989]. Room temperature calibrations are accurate to ±1 GPa at 14 GPa [*Ohtani and Kumazawa*, 1981]. Precision is probably within ±0.1 to 0.2 GPa, on the basis of phase changes that can be observed over these small increments of pressure.

A pressure calibration scale at high temperatures is more difficult to determine. However, existing measurements show that high temperatures require a greater press load to achieve a specific pressure in the sample [*Ito and Yamada*, 1982; *Gasparik*, 1989]. Pressures reported in Table 2 are for both room temperature and high-temperature calibrations. Pressures indicated in all the figures are based on the high-temperature calibrations only.

2.6. *Effect of Pressure on Thermocouple emf*

This effect is an important unknown because measurements have only been made to consider its absolute effect at pressures less than 3 GPa [*Getting and Kennedy*, 1970]. For Pt/Rh thermocouples it was estimated that the temperatures will be too low by 28°C at 5 GPa and 2000°C [*Getting and Kennedy*, 1970]. At 1750°C and 9 GPa, W/Re thermocouples read the same temperature as Pt/Rh [*Kato and Kumazawa*, 1985*a*], indicating that W/Re thermocouples also read too low. The effect of pressure of emf is nonlinear. On the basis of the polynomial fit offered by *Getting and Kennedy* [1970], the temperatures reported here may be too low also. There is a limit, however, to how large this error is likely to be. An error as high as 200°C at 15 GPa is not plausible because it would yield a fusion curve of forsterite that is perfectly straight (Figure 11), rather than curved as it must be.

2.7. *Anhydrous Experiments*

Water is contained in the assemblies as free water along grain boundaries and as $Mg(OH)_2$ and can be difficult to expel. In an attempt to ensure that all the samples were anhydrous, the entire high-pressure assembly was fired at 1050°–1100°C for 1–2 hours immediately prior to running the experiment. Drying was done in an argon atmosphere in order to prevent oxidation of the thermocouples and graphite heaters. No hydrous phases were observed in these experiments.

2.8. *Time*

Run durations varied from 0.2 to 8.0 min (Table 2). Longer-duration experiments are not feasible for Mo containers because of decrepitation of the heater. Indeed, 3 min is usually the maximum run time permitted with assembly C because the silica melt digests the molybdenum container and reacts with the lanthanum chromite heater.

A reversal experiment is reported below, indicating that chemical equilibrium is attained between silicate liquid and garnet in the 3-min duration at 2185°C. Melting itself occurs almost instantly, on the basis of experiments that have been quenched immediately upon heating to the desired temperature. We expect that equilibrium is usually reached within the first minute of an experiment at temperatures in the 2000°C range. This is fortunate because we are concerned that Soret diffusion, gravitational separation of liquid from crystals, and saturation gradient chemical diffusion may become problems in experiments that are longer in duration than about 10 min.

3. EXPERIMENTAL RESULTS

Experimental results are summarized in Table 2. Polished thin sections were made for each experiment, and phase

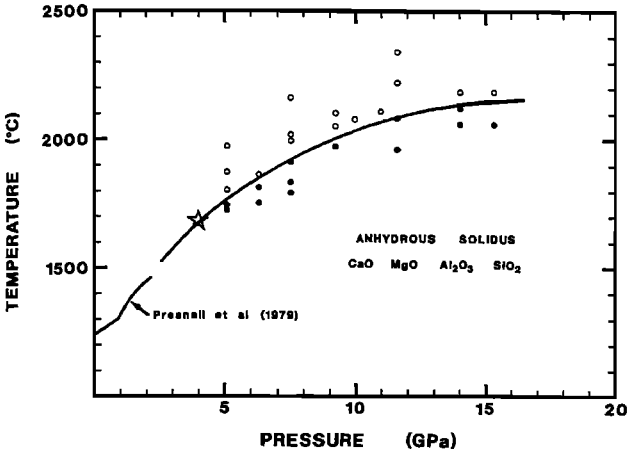

Fig. 4. Anhydrous solidus in the system CaO-MgO-Al_2O_3-SiO_2 determined from experiments on both komatiite (K) and peridotite (P). The open star is the solidus determined by *Davis and Schairer* [1965] at 4 GPa. Symbols are defined as follows: open circles, all liquid; solid circles, all crystalline; and half-solid circles, crystals plus liquid.

identification was made using backscatter scanning electron microscopy and the electron microprobe, using wavelength dispersive spectrometry on a JEOL 8600 machine. The phase assemblages in Table 2 are reported for three temperature conditions. In the middle column are the phase assemblages observed at the temperature recorded by the thermocouple (*Tc*). In the first and last columns are the phase assemblages observed up temperature ($T > Tc$) and down temperature ($T < Tc$) along the gradient in the heater. Most experiments therefore yield portions of an isobaric phase diagram.

For the komatiite (K) the liquid phase quenched to a mixture of very fine quench crystals, usually barred and hopper olivine in addition to lesser amounts of glass. For the peridotite (P), chondrite (C), and KLB1 compositions the liquid phase was invariably preserved as fine and sometimes very coarse quench crystals consisting of barred olivine, Ca-rich pyroxene, and other phases too small to identify. Indeed, we often found it impossible to identify primary from quench clinopyroxenes using backscatter scanning electron microscope images, examples of which are shown in Figures 7 and 9. Quench clinopyroxenes can form as large compositionally uniform grains (80 μm; Figure 8). However, they typically contain 9–10% Al_2O_3. Although these alumina contents can be stable in the 2-GPa range, they should drop to around 1–2% at pressures of 10 GPa and more [*Gasparik*, 1989] (see below), demonstrating that many primary-looking clinopyroxenes are in fact formed during the quench.

3.1. *The Anhydrous Solidus in the System CaO-MgO-Al_2O_3-SiO_2*

A plot of all data for the komatiite and peridotite compositions is shown in Figure 4. The data appear to share a common anhydrous solidus, and the curve shown can be described by the equation

$$T\,°C = 1263 + 123.7P - 5.36P^2 + 0.069P^3$$

where P is in units of gigapascals. A second-order polynomial gives an equally good fit to our data in the entire 5- to 15-GPa range but predicts temperatures that are somewhat higher than those reported by *Presnall et al.* [1979] at 2 GPa. The solidus also compares very favorably with the 4-GPa result reported by *Davis and Schairer* [1965] (1680°C). Although the agreement is very good, differences are to be anticipated because komatiites and peridotites solidify to orthopyroxene-free assemblages of Ol + Cpx + Gt at high pressures. Melting is not strictly invariant, except at thermal minima (see below). However, these differences are small and difficult to resolve experimentally.

The slope of the solidus is reduced by an order of magnitude with increasing pressure from about 130°C GPa^{-1} near the 2.2-GPa cusp to about 13°C GPa^{-1} at 15 GPa. There is no evidence for a negative slope to the solidus.

3.2. *Phase Relations for Komatiite*

The liquidus phase relations are summarized in Figure 5. Olivine is the liquidus phase at 5.1 GPa, and the crystallization sequence is L, L + Ol, L + Ol + Gt, L + Ol + Gt + Cpx, Ol + Gt + Cpx. A shorthand notation for this isobaric sequence can be written L-Ol-Gt-Cpx.

In experiment K-15 at 6.3 GPa, garnet is the liquidus phase, but the area in the charge occupied by L + Gt is restricted to a very narrow band of about 30 μm thick at the sample/heater contact where the temperature gradient is highest. Most of the charge consists of olivine coexisting with garnet and liquid (L + Gt + Ol), and clinopyroxene appears near the solidus. The crystallization sequence at 6.3 GPa is L-Gt-Ol-Cpx. The komatiite must be multiply saturated in olivine and garnet (L + Ol + Gt) at some pressure slightly less than 6.3 GPa. At higher pressures the liquidus field for garnet (L + Gt) expands considerably, as seen by increasing portions of experimental charges occupied by liquid and garnet.

The liquidus temperature for komatiite at 1 atm is calculated to be 1600° ± 30°C by the method of *Herzberg* [1979]. The actual liquidus temperatures for olivine at higher pressures were not bracketed. The *T-P* curve for the olivine liquidus in Figure 5 was drawn from the 1-atm temperature parallel to the fusion curve of forsterite. We show from the experimental data on the peridotite composition (P) that this is an excellent approximation. The temperature interval

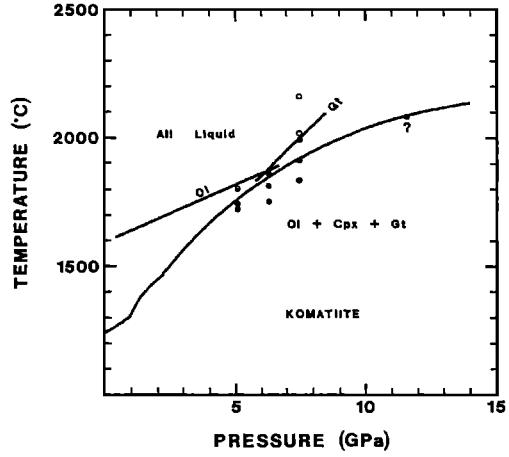

Fig. 5. Experimental results on komatiite (K). Solidus is from Figure 4.

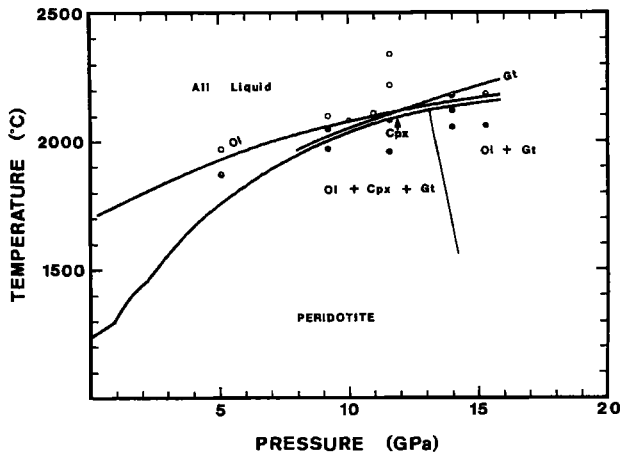

Fig. 6. Phase relations for peridotite (P). The negative slope of the subsolidus boundary separating Ol + Cpx + Gt from Ol + Gt is from *Gasparik* [1989].

between the liquidus and the solidus at 7.5 GPa is less than 100°C and is 360°C at 1 atm. At 6.3 GPa it is less than 50°C (Figure 5).

3.3. *Phase Relations for Peridotite*

The liquidus phase relations are summarized in Figure 6. Olivine is the liquidus phase at pressures up to 11 GPa. Down the temperature gradient, olivine is joined by garnet (Figure 7), quench clinopyroxene (Figure 8) and finally by primary clinopyroxene (Figure 9) on the solidus. The crystallization sequence is usually L-Ol-Gt-Cpx. However, at 5.1 GPa a few grains of orthopyroxene were observed, yielding the sequence L-Ol-Gt-Opx-Cpx.

At 14 GPa the liquidus phase is garnet, and this is seen as a narrow band consisting of L + Gt in Figure 10. At slightly lower temperatures, olivine appears and crystallizes together with garnet to the solidus.The complete isobaric crystallization sequence is L-Gt-Ol (Figure 10). The separate phases of clinopyroxene and garnet that coexist at 11.6 GPa become totally dissolved into a single garnet phase that is majoritic somewhere between 11.6 and 14 GPa. At 15.3 GPa the liquidus phase remains garnet, and the crystallization sequence is identical to that at 14 GPa (L-Gt-Ol). The main difference is that the band containing L + Gt is much wider, demonstrating the effect of pressure on expanding the thermal stability of garnet.

Olivine liquidus temperatures are shown again in Figure 11 together with the fusion curve of forsterite [*Ohtani and Kumazawa*, 1981] and a Stony Brook melting experiment on forsterite at 2350°C and 16.5 GPa [*Presnall and Gasparik*, this issue]. The Stony Brook experiment indicates that the curve determined by *Ohtani and Kumazawa* [1981] should bend slightly more, but the modified curve is located within their ± 100°C error bar. It is demonstrated that olivine liquidus temperatures in CaO-MgO-Al_2O_3-SiO_2 approxi-

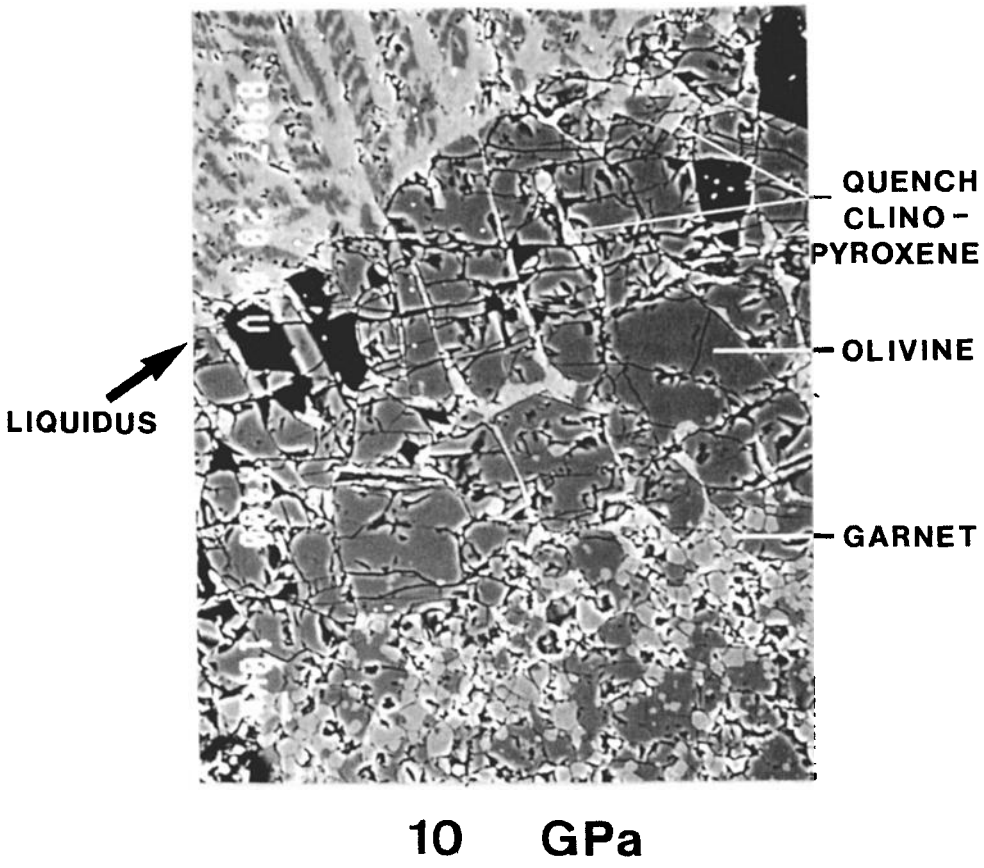

Fig. 7. Experimental charge of peridotite at P = 10 GPa and T = 2080°C (P-16; backscatter scanning electron microscopy). The band in the middle is bimineralic and consists of large olivine crystals separated by slivers of quench clinopyroxene. Garnet appears at lower temperatures, down the temperature gradient.

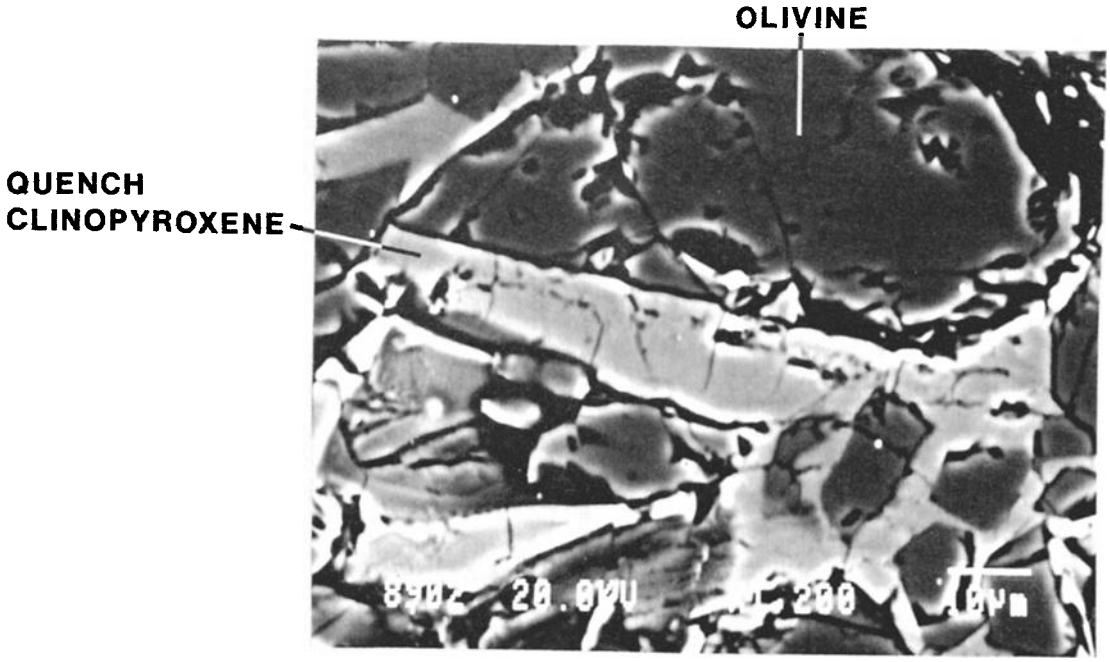

Fig. 8. Close-up of quench clinopyroxene from P-16.

mately parallel the fusion curve of forsterite determined by *Ohtani and Kumazawa* [1981], and they precisely parallel the modified fusion curve offered in Figure 11. CaO and Al_2O_3 depress the stability of pure forsterite by about 200°C at 1 atm, an amount seen also at pressures up to 15 GPa. This is evidence that in general, a fusion curve for a single-component system may be an excellent guide to liquidus curves in multicomponent systems [*Herzberg*, 1983; *Herzberg and O'Hara*, 1985].

The geochemistry of garnet varies considerably with temperature. Detailed electron microprobe analyses were made of the garnets and olivines dispersed between the hot and cold ends of P-12, and representative analyses are given in Table 3. The strongest changes that occur are for CaO and Al_2O_3, and these are shown in Figure 12. Lime increases from 3% at the liquidus to around 11% near the solidus, while alumina decreases by lesser amounts. This translates to a change in CaO/Al_2O_3 from 0.17 at the liquidus to 0.84 at the solidus, and it occurs through a temperature range of around 100°C.

Garnet crystals located near the solidus are majoritic and show the greatest variability; this is interpreted as arising from a reduced liquid volume that is necessary for equilibrium diffusion to occur. However, the solidus garnets observed are in excellent agreement with solidus garnets predicted from a criterion for equilibrium. The equilibrium compositions of olivine and garnet, the only two phases that are stable at subsolidus conditions, are constrained to lie on a tie line that includes the bulk composition (P; this is valid also at the solidus). This is evidence indicating that equilibrium was indeed obtained during the 3-min duration of the experiment, and it supplements additional evidence described below.

Lime and alumina contents of high-temperature olivines, those which appear with liquid and garnet at the hot end, are typically about 0.25% (Figure 12). However, low-temperature olivines, those near the solidus, have contents of lime that exceed 0.5%, while alumina drops to about 0.1%.

Mass balance requires that composition of the liquid coexisting with olivine and garnet on the solidus at 14 GPa has MgO and CaO/Al_2O_3 higher than the bulk composition itself. The bounds are MgO $\geq$ 42%, CaO and Al_2O_3 falling somewhere in the stippled region of Figure 12, and $CaO/(CaO + Al_2O_3) \geq 0.47$.

3.4. *Equilibrium*

For most melting experiments in the 2000°C range the quoted duration of the experiment is typically less than 3 min [e.g., *Takahashi*, 1986; *Ohtani et al.*, 1986] (see also this paper). We found that 3 min is the maximum time possible for a molybdenum capsule that contains a large volume fraction of liquid (e.g., Figure 3; 2155°C). However, run times of up to 6 min are possible if the melt fraction is reduced (e.g., Figure 3; 2050°C). Longer experiments with molybdenum capsules are not possible because the of the high solubility of molybdenum in silicate melts. The container becomes digested, and the melt leaks to the lanthanum chromite heater, resulting in a loss of resistivity control. This problem is overcome with rhenium capsules, but graphite/diamond capsules seem to leak as well because of the common occurrence of heater failure in experiments that contain a lot of melt.

We therefore attempted a reversal experiment in order to determine if equilibrium between crystals and silicate melt can be obtained in 3 min for a temperature of 2185°C (P-15). This experiment was identical to run P-12 which contains garnet as the liquidus phase, except that seeds of both pyrope and grossular were mixed in the sample with the intention of growing majoritic garnet rims on them; rims grown on both seeds that overlapped in composition would be a positive test for equilibrium [e.g., *Gasparik*, 1989].

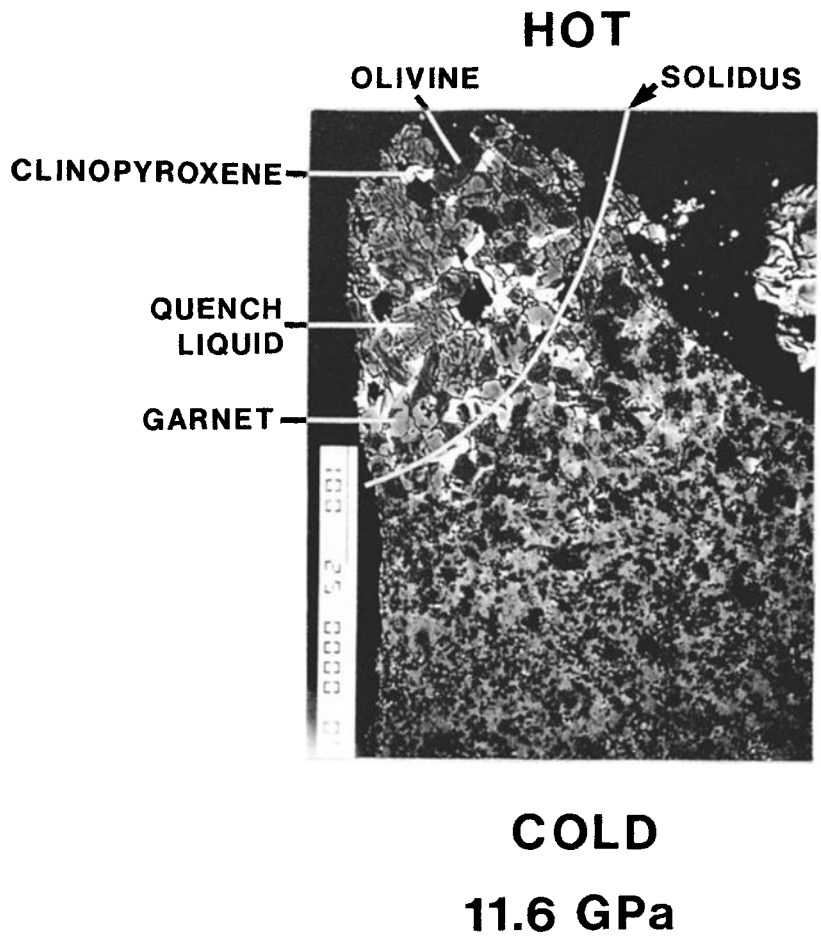

Fig. 9. Experimental charge of peridotite at $P = 11.6$ GPa and $T = 2080$°C (P-02). This is a solidus phase assemblage (L + Ol + Cpx + Gt), and individual crystals of olivine, garnet, and clinopyroxne can be seen separated by quench liquid. Electron microprobe analyses of clinopyroxenes and garnets are given in Table 3. The thermocouple junction was sandwiched between the fine-grained part of the charge and the thermocouple ceramic (white patch in the top right), yielding a subsolidus result.

The results are shown in Figures 13 and 14. It was found that garnet rims grew only on the pyrope seeds and that no grossular seeds coexist with liquid. Relict grossular seeds could be found in abundance, but only at the cold part of the charge below the solidus. Apparently, the grossular seeds either melted completely or were assimilated into the garnets.

Garnet remains the liquidus phase, but it was found to grow with two distinct morphologies. Small garnet nuggets measuring 10–15 μm across occur (Figures 13 and 14), and these are typical of those seen in experiments without seeds (Figure 10). However, large rims of garnet were also found, and these grew only on the pyrope seeds (Figures 13 and 14). The rims were sufficiently large to display a weak birefringence, demonstrating the noncubic nature of these "garnets" [*Kato and Kumazawa*, 1985*b*; *Sawamoto*, 1987] which formed by Mg-Si ordering during the quench [*Hatch and Ghose*, 1989]. Furthermore, the rims invariably grow on the hot side of each pyrope seed. The rim-seed contact is highly corroded in some cases (Figure 13, top). However, other contacts are very sharp, and Figure 14 shows that the outline of the original euhedral pyrope seed is well preserved. The cold sides of all pyrope seeds are variously corroded, in some cases with deep embayments containing liquid (Figure 13, bottom).

Electron microprobe analyses of the garnet nuggets and rims are shown in Figure 15. In general, the compositional trend is similar to that observed for the unseeded run (P-12) in that CaO/A_2O_3 changes considerably with temperature from the liquidus to the solidus. However, the trend is offset, and the garnets in it display higher absolute values of CaO and Al_2O_3 (Figure 15). These enrichments are in pyrope and grossular compositional vectors, and they demonstrate how changes in bulk composition contributed to the changes in the composition of garnet. Lime was added by the total dissolution of grossular seeds, as indicated by the total absence of these seeds in the presence of melt. The partial dissolution of pyrope seeds contributed additional alumina, as indicated by the severely corroded outlines in Figures 13 and 14.

It is clear that both composition and temperature must contribute to the variations in CaO/Al_2O_3 of garnet seen in Figure 15. Fortunately, a pyrope seed with a thick rim of garnet was found precisely on the liquidus (Figure 14), and this has permitted the effects of temperature to be filtered out. The results are shown in Figure 16. It can be seen that

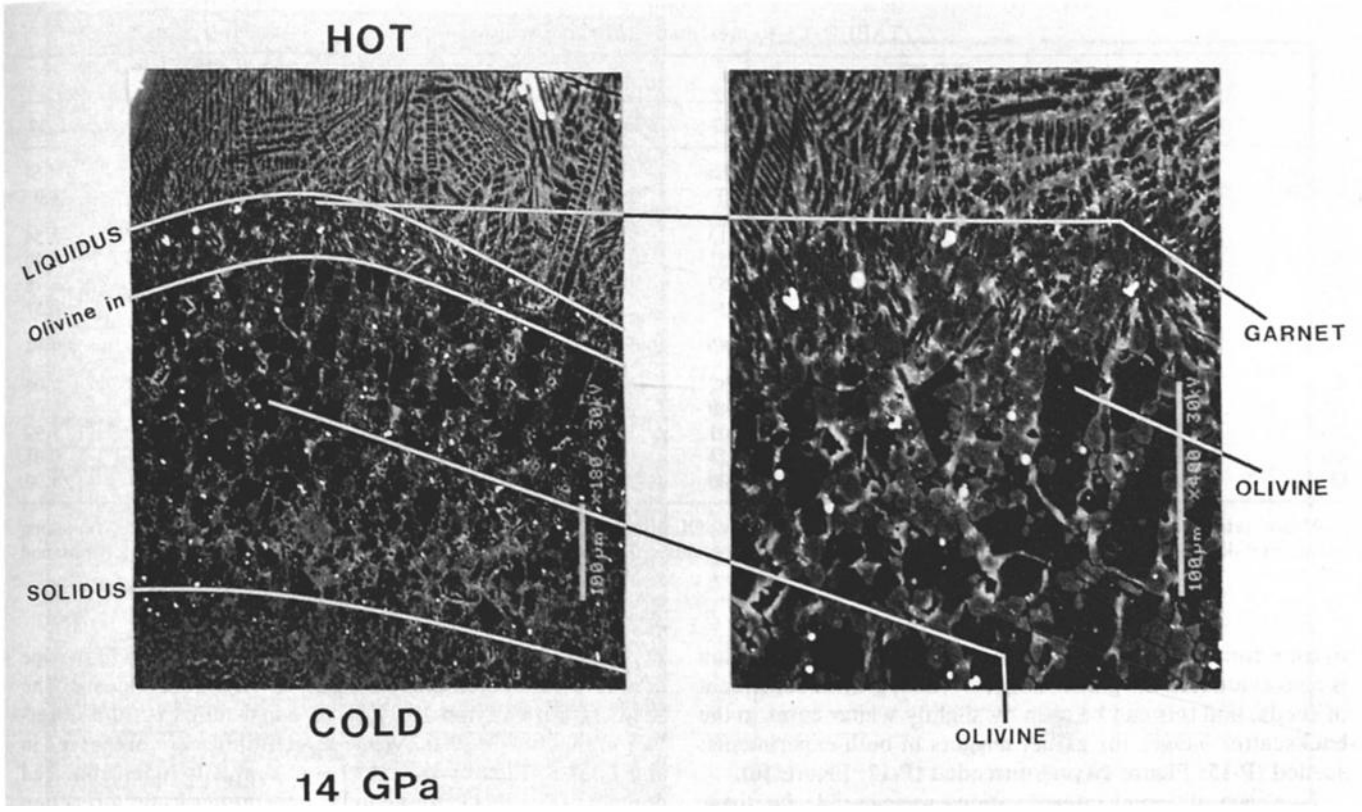

Fig. 10. Experimental charge of peridotite at $P = 14$ GPa and $T = 2185$°C (P-12). Interstitial liquid (quench) occurs with garnet and olivine, although it is likely that some has been expelled to the hot end of the charge. Electron microprobe analyses of garnets and olivines from the liquidus to solidus are given in Table 3 and Figure 12. Note the alignment of olivine crystals (C axes) along the temperature gradient.

a range of compositions exists for liquidus garnets, but it is quite limited. For the unseeded run (P-12), variations in lime and alumina within garnet grains are equal to variations between garnet grains; the total variation is quite small, about 1% for both CaO and Al_2O_3. These compare with the seeded run with absolute lime contents from 3 to 5% (more typically 3–4%) and alumina contents from 18 to 20%. We are impressed by how homogeneous these liquidus majorites actually are, considering that the duration of each experiment was only 3 min, and we regard this as evidence indicating a strong approach to equilibrium at 2185°C. Equally important is how the liquidus garnet nuggets compare to the liquidus garnet rim (Figure 14). They are virtually indistinguishable, indicating that nucleation creates no barrier to equilibrium.

Most of the variability in lime and alumina for the liquidus garnet rim (Figure 14) occurs systematically from the inner to the outer portions of the rim, and this is shown in Figure 17. The garnet rim is paradoxically zoned with the lowest pyrope contents next to the pyrope seed and the highest

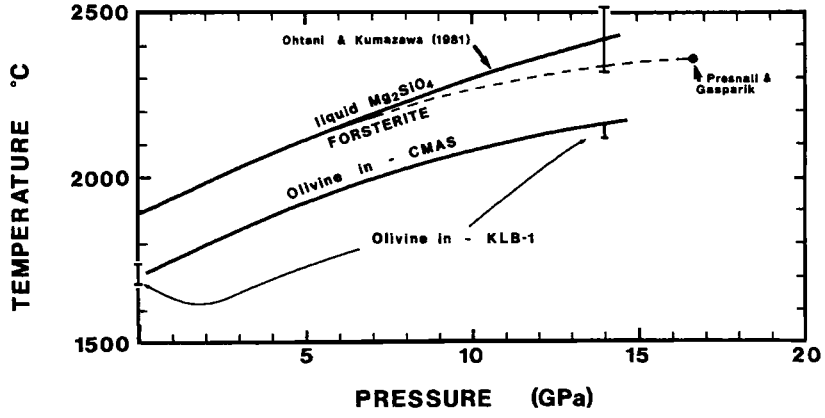

Fig. 11. Olivine liquidus temperatures and pressures for peridotite (P) (Figure 6) compared to the fusion curve of forsterite [*Ohtani and Kumazawa*, 1981]. The dashed curve is a modified version of the fusion curve of forsterite, based on a Stony Brook experiment [*Presnall and Gasparik*, this issue]. KLB1 liquidus at 14 GPa is a Stony Brook determination; liquidus at 1 atm is calculated.

TABLE 3. Representative Mineral Analyses

	Run										
	K-15	K-12	P-02	P-02	P-12	P-12	P-12	P-12	P-12	P-12	P-12
Phase	Gt-Lq	Gt-Lq	Gt-Sl	Px-Sl	Gt-Lq	Gt1	Ol1	Gt2	Ol2	Gt-Sl	Ol-Sl
P, GPa	6.3	7.5	11.6	11.6	14.0	14.0	14.0	14.0	14.0	14.0	14.0
SiO_2	45.03	46.54	49.52	55.38	49.13	48.23	43.00	50.23	43.11	49.74	42.54
Al_2O_3	21.91	19.54	15.99	1.45	17.51	16.82	0.21	15.03	0.16	13.34	0.10
MgO	27.44	28.81	30.31	22.33	29.87	30.07	56.71	28.25	56.89	27.25	56.78
CaO	5.34	4.82	4.20	20.37	3.34	3.93	0.27	6.85	0.36	10.30	0.51
Total	99.72	99.71	100.03	99.54	99.85	99.05	100.19	100.36	100.52	100.63	99.93
Si	3.08	3.17	3.36	3.95	3.32	3.30	1.00	3.42	1.00	3.42	1.00
Al	1.77	1.57	1.28	0.12	1.40	1.36	0.01	1.20	0.00	1.08	0.00
Mg	2.80	2.93	3.06	2.37	3.01	3.07	1.98	2.86	1.98	2.79	1.99
Ca	0.39	0.35	0.31	1.55	0.24	0.29	0.01	0.50	0.01	0.76	0.01
O	12.00	12.00	12.00	12.00	12.00	12.00	4.00	12.00	4.00	12.00	4.00

Abbreviations are defined as follows: Gt, garnet; Px, pyroxene; Ol, olivine; Lq, liquidus; and Sl, solidus. Gt1-Ol1 represents coexisting garnet and olivine pairs at "olivine in" temperature. Gt2-Ol2 represents coexisting garnet and olivine between "olivine in" temperature and solidus.

pyrope content furthest from the pyrope seed. This zonation is also evident in the garnet nuggets which grew independent of seeds, and this can be seen by slightly whiter cores in the backscatter images for garnet nuggets in both experiments: seeded (P-15; Figure 14 and unseeded (P-12; Figure 10).

Two very different interpretations are possible for these zonations, depending on the growth mechanism of garnet, and these provide insights into the diffusion distances involved. In the first the garnet rims grew outward on the pyrope seeds. This is consistent with similarly zoned garnet nuggets that grew without seeds. The high-CaO inner rim represents garnet grown "early," the source of the lime being instantaneously dissolved grossular seeds. The outer rim represents garnet grown "late" and is enriched in a pyrope component because of the slow dissolution of pyrope seeds, which takes place largely on the cold sides of the seeds (Figure 13 and 14). This is consistent with the observation that the original pyrope seed outlines are preserved in some cases (Figures 14 and 13, bottom). Corroded rim-seed contacts (Figure 13, top) can be interpreted to be a reaction confined to a small volume near the original surface of the seed. In this outward garnet growth model the diffusion distances for CMAS components in the melt phase are considerable and would be of the order of one tenth of 1 mm in 3 min.

The second model involves inward growth of garnet from the surface of the original seed. Growth proceeds inward via a thin film of silicate melt, with dissolution occurring at the

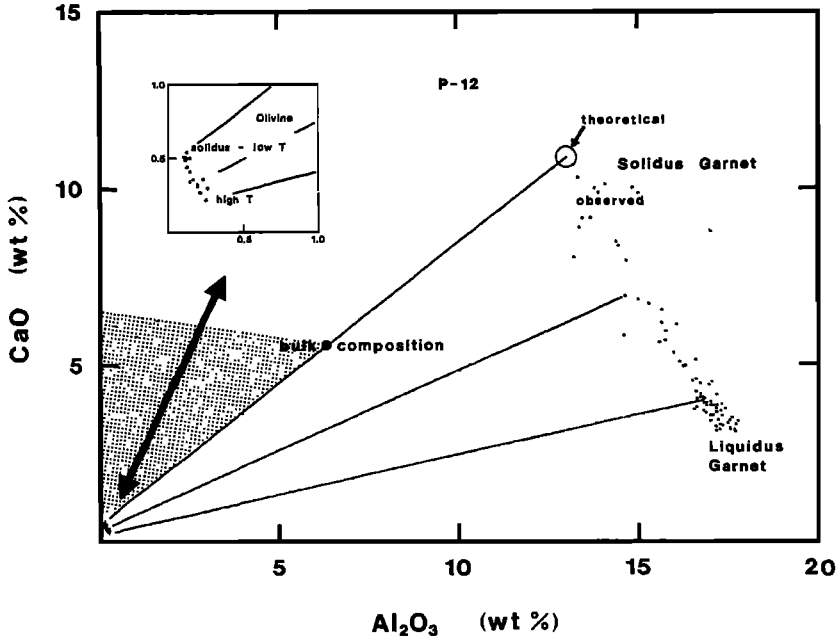

Fig. 12. Lime and alumina contents of garnet and coexisting olivine along the temperature gradient in experiment P-12 (Figure 10). A criterion for equilibrium is that garnets and olivines on the solidus must lie on a tie line which contains the bulk composition; this defines a "theoretical" solidus garnet that is very close in composition to those actually observed.

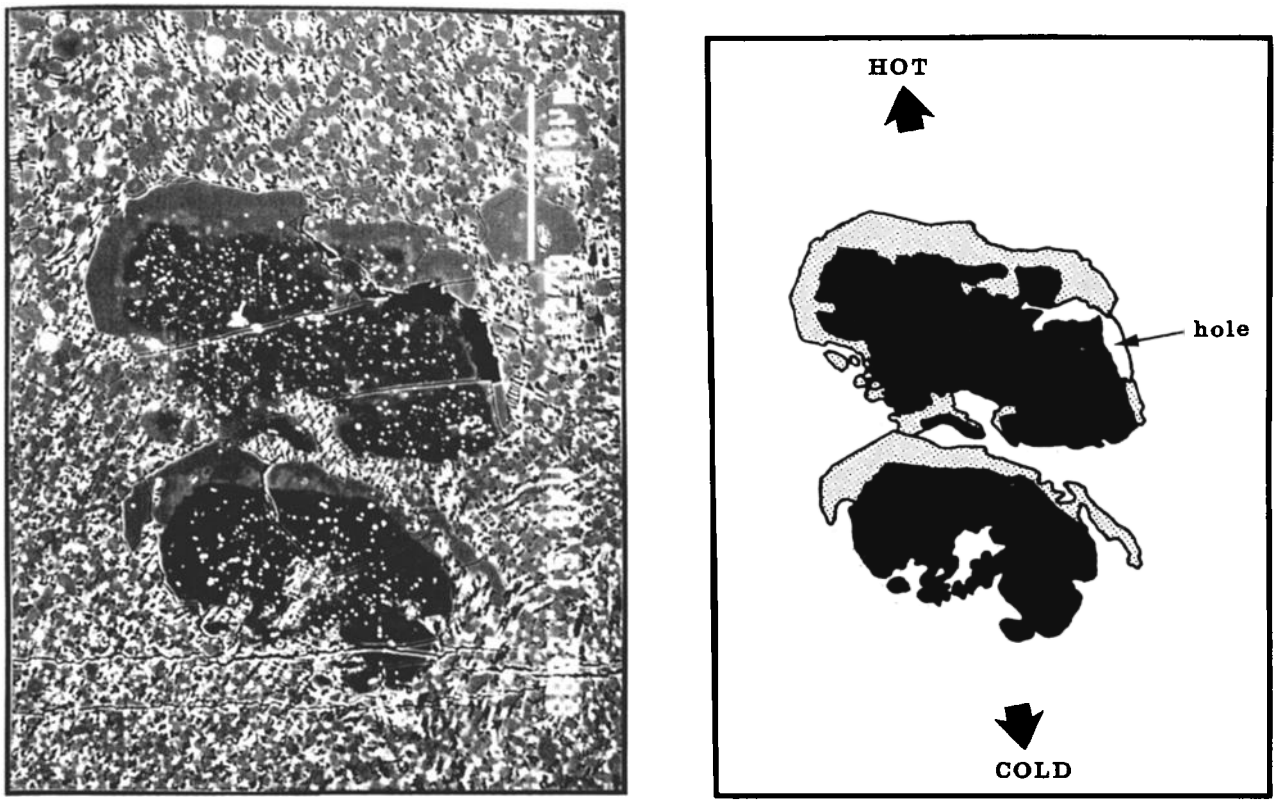

Fig. 13. Reversal experiment (P-15) showing rims of garnet that invariably grow on the hot sides of pyrope seeds. The garnet-pyrope contact is sometimes corroded (top) and sometimes uncorroded (bottom). The cold sides of pyrope seeds are invariably embayed and filled with liquid.

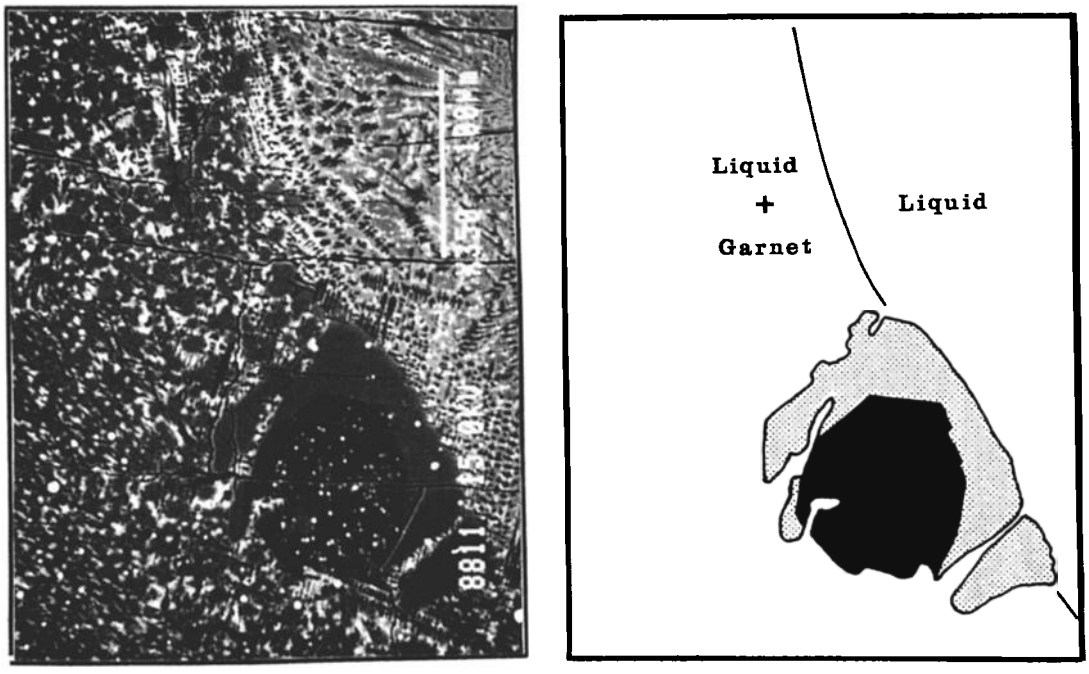

Fig. 14. Another seed and rim in P-15, showing an original euhedral pyrope seed outline and the growth of a garnet rim on the liquidus. Electron microprobe analyses of both the small garnet nuggets and the garnet rim are given in Figure 16.

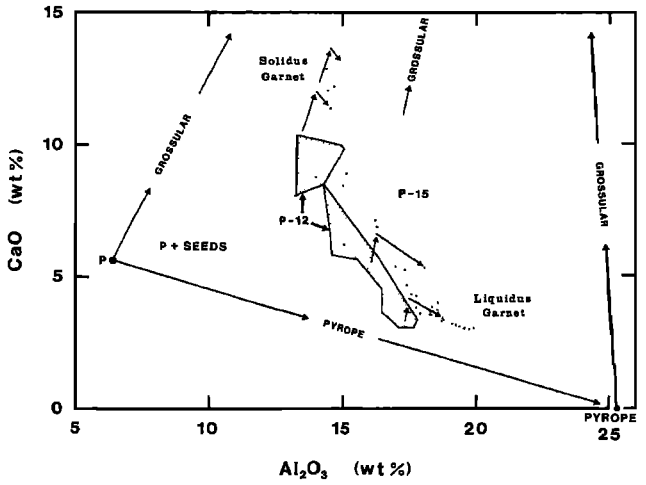

Fig. 15. Lime and alumina contents of garnets in reversal experiment P-15 compared to the unseeded experiment (P-12: Figure 12). Compositional vectors demonstrate the effect of the pyrope and grossular seeds in modifying both the bulk composition and the garnets that crystallize from it (Figure 12).

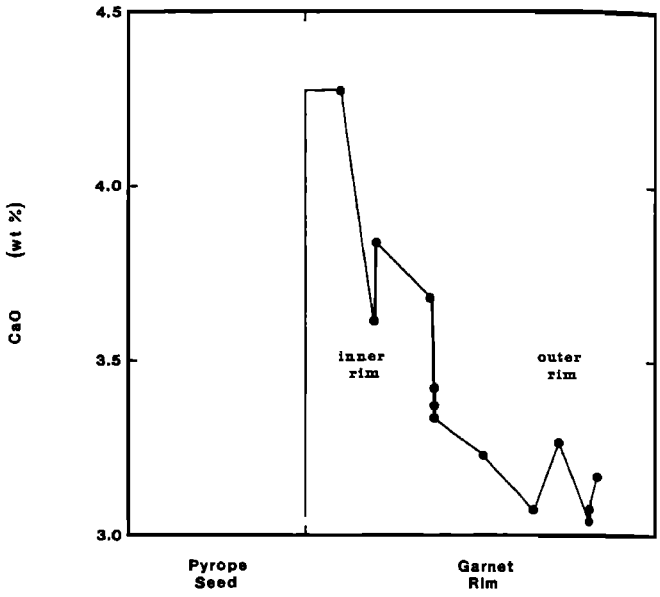

Fig. 17. Zoned lime content of the garnet rim in Figure 14.

seed-melt contact and precipitation occurring at the melt-rim contact. The high-CaO inner rim arises from this trapped liquid, and the corroded rim-seed contacts (Figure 13, top) represent an arrested stage in this digestion-repreciptation process. Figures 13 and 14 could be interpreted as partial pseudomorphs after pyrope. This inward growth model is very similar to that observed in reversal experiments involving seeds and fluxes in experiments at 1600°C [*Gasparik*, 1989].

The outward growth model is also consistent with a true reversal experiment because the dissolution of the two seeds can be seen to make an observable geochemical contribution to the precipitating garnet. We conclude, therefore, that the time required for equilibrium to occur between silicate crystals and melt at 2185°C is less than or equal to 3 min.

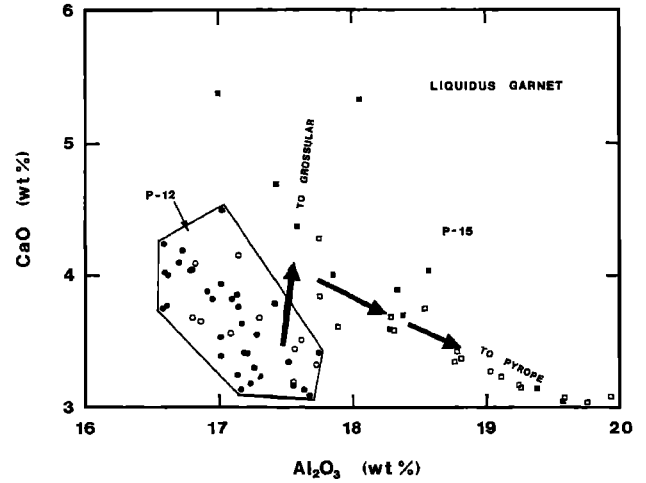

Fig. 16. Liquidus garnets in both the unseeded run (P-12) and the run seeded with pyrope and grossular seeds (P-15). Open circles are points analyzed within a single large garnet grain; solid circles are for all garnet grains. Open squares are points within the single large garnet rim shown in Figure 14; solid squares are for individual garnet nuggets along the liquidus in Figure 14.

Additional evidence for equilibrium is seen in experiments done on the chondrite composition (below).

3.5. *Phase Relations for Chondrite*

The liquidus phase relations and crystallization sequences for chondrite are somewhat more complicated, as is shown in Figure 18. The liquidus phase is olivine below 10 GPa and garnet above, in agreement with the data of *Ohtani et al.* [1986] on another chondrite analogue composition. However, orthopyroxene is also an abundant crystallizing phase at pressures less than about 12 GPa. Experiments run at 4 min form wide bands of orthopyroxene that poikilitically enclose garnet (Figure 19). Where clinopyroxene appears, it is invariably at the solidus (Figure 19). Compositions of coexisting garnet, orthopyroxene, and clinopyroxene at the solidus are given in Table 4. These are almost identical to those predicted by *Gasparik* [this issue] from reversal experiments done at much lower temperatures, providing yet additional evidence that equilibrium occurs within minutes at temperatures above 2000°C.

Our experiment 16.5 GPa yielded the first reported occurrence of an anhydrous form of phase B [*Herzberg and Gasparik*, 1989]. This form grows as very large crystals (Figure 20) and has a stoichiometry that is similar to

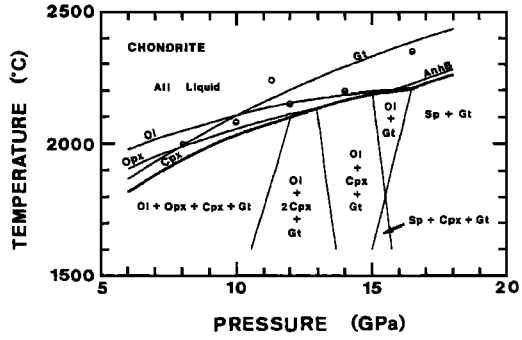

Fig. 18. Phase relations for chondrite.

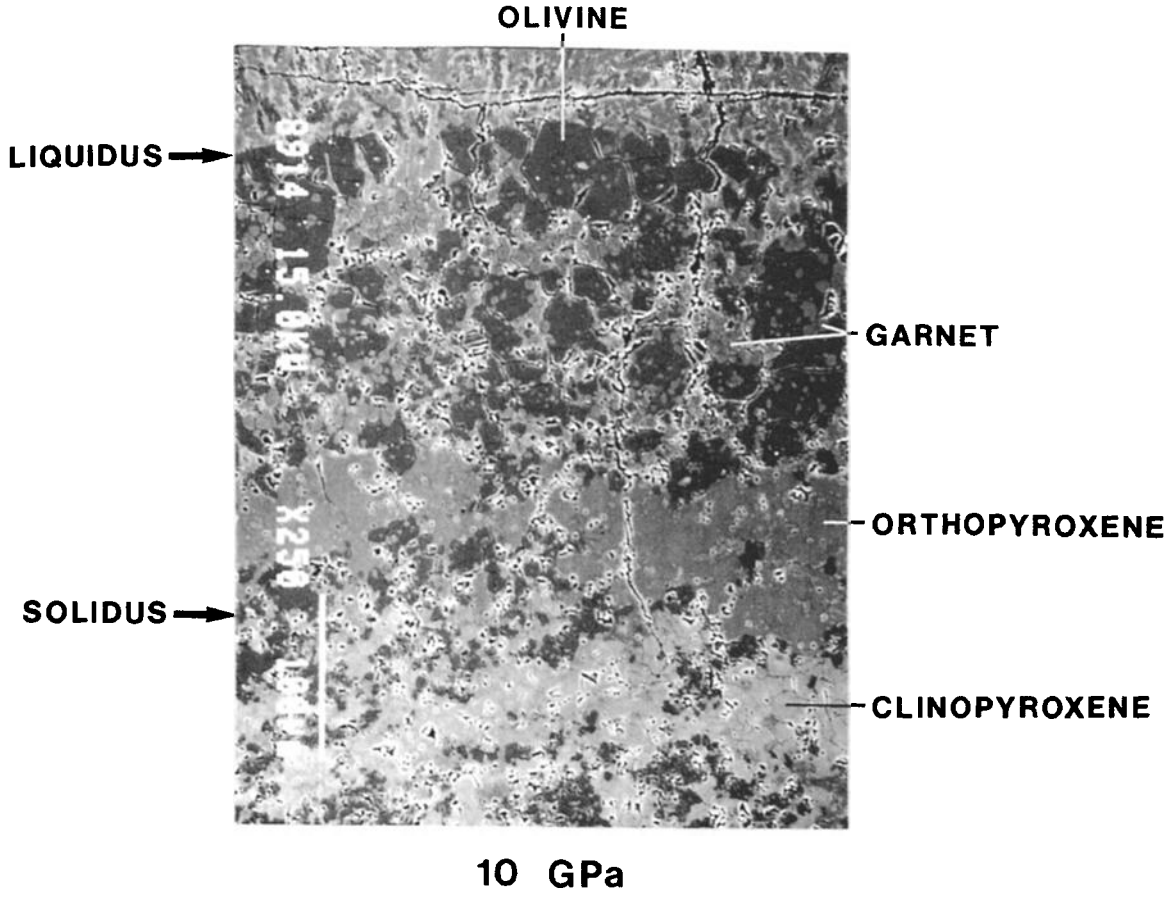

Fig. 19. Experimental charge of chondrite at $T = 2080°C$ and $P = 10$ GPa (C-05). Expulsion of intergranular liquid and grain coarsening occur along the temperature gradient in long-duration experiments, producing the bands of olivine and orthopyroxene (see text). Garnet nuggets occur as homogeneously dispersed crystals poikilitically enclosed by olivine and orthopyroxene, but some clumping in aggregates also occurs.

$Mg_{14}Si_5O_{24}$ (Table 4). *Finger et al.* [1989] determined that it has a crystal structure and stoichiometry similar to the more familiar phase B, $Mg_{12}Si_4O_{19}(OH)_2$ and called it phase AnhB.

In our experiment, phase AnhB can be seen to coexist with liquid and majorite garnet in a very restricted area of the charge near the solidus, separating the fields of L + Gt and L + Gt + Sp (Figure 20). *Kato and Kumazawa* [1986] and *Ito and Takahashi* [1987] reported phase B in a similar distribution from experiments on natural peridotite compositions. It is now likely that what they had synthesized was phase AnhB, rather than phase B. *Kato and Kumazawa* [1986]

TABLE 4. Representative Mineral Analyses

	Run							
	C-5	C-5	C-5	C-3	C-3	C-3	C-3	C-3
Phase	Cpx	Opx	Gt	Gt1	Q-Sp	Gt2	Sp	AnhB
P, GPa	10	10	10	16.5	16.5	16.5	16.5	16.5
SiO_2	58.16	58.59	47.69	53.75	41.63	55.45	42.74	34.38
Al_2O_3	1.08	1.02	19.14	10.41	2.17	5.49	0.54	0.67
MgO	32.43	37.68	29.38	33.60	55.85	34.18	56.49	65.38
CaO	8.43	2.34	3.71	1.59	0.06	4.25	0.05	0.04
Total	100.10	99.63	99.92	99.35	99.72	99.37	99.82	99.82
Si	1.987	1.979	3.234	3.630	0.977	3.778	1.002	4.930
Al	0.043	0.041	1.529	0.829	0.060	0.441	0.015	0.115
Mg	1.652	1.897	2.969	3.382	1.954	3.472	1.973	13.968
Ca	0.309	0.085	0.270	0.115	0.002	0.310	0.001	0.005
O	6.000	6.000	12.000	12.000	4.000	12.000	4.000	24.000

Abbreviations are defined as follows: Gt1, liquidus garnet; Gt2, solidus garnet; Q-Sp, quench modified spinel; Sp, modified spinel; and AnhB, phase anhydrous B.

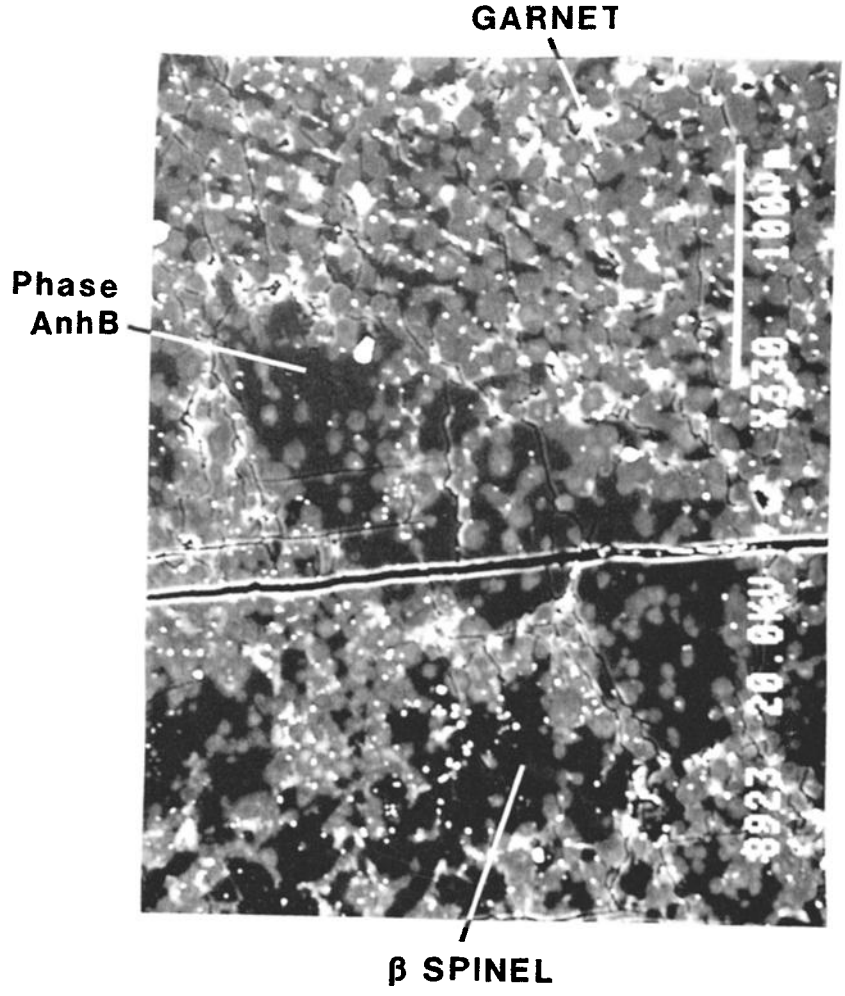

Fig. 20. Experimental charge of chondrite at 16.5 GPa (C-03). Phase AnhB grows as very large crystals poikilitically entraining garnet. Liquid coexisting with garnet at the top quenches to elongated crystals of modified spinel (Mg_2SiO_4; solid semiradiating crystals) that can grow over 0.5 mm in length and that have over 2% Al_2O_3 (Table 4). Primary modified (β) spinel is also seen at the bottom.

interpreted this distribution as indicating incongruent melting of modified spinel, and this is fully compatible with our experimental results. The reaction is as follows: modified spinel = phase AnhB + liquid.

3.6. *Melting Experiments on a Natural Peridotite at 14 GPa*

The liquidus phase at 14 GPa is garnet, but it is soon followed by olivine several tens of microns distance down the temperature gradient, indicating that KLB1 is close to being multiply saturated in olivine and garnet at this pressure. Garnet and olivine crystallize together with liquid until the solidus is reached, where they are joined by clinopyroxene. The crystallization sequence is thus L-Gt-Ol-Cpx.

A metal phase is present throughout. Its abundance and composition are different above and below the solidus (see Figure 2). Above the solidus it usually occupies 10–20% of the liquid portion charge; however, it can reach 50% in isolated locations, becoming an intercumulus-looking melt of almost pure metal engulfing large crystals of olivine and garnet. It is a heterogeneous Mo-Fe alloy that is most enriched in Mo nearest the molybdenum container. In the charge located below the solidus, the metal is Fe-rich; the droplets are not as abundant, and they are distributed in necklaces rimming grains of relict spinel from KLB1, the source of the Fe. Original grains of spinel are clearly refractory survivors; they decrease in number from the cold to the hot end of the charge, and the odd grain can still be seen above the solidus. Some Mo was observed in these Fe-rich metal necklaces below the solidus, indicating that it was transported there as a vapor.

The solidus has been tightly bracketed between 2020°C and 2050°C, and the liquidus has been bracketed between 2115°C and 2155°C, a temperature contrast of about 100°. This compares with a temperature contrast of about 500° at 1 atm [*Takahashi*, 1986]. At small increments between these temperature bounds the liquidus and solidus can be observed to sweep down the temperature gradient (Figure 3).

The solidus for KLB1 is compared with others in Figure 21. Our determination at 14 GPa is about 150° higher than the KLB1 solidus reported by *Takahashi and Scarfe* [1985] and *Takahashi* [1986]. There are two possible explanations for this discrepancy. The first may be due to small amounts of water that were not successfully removed in the drying

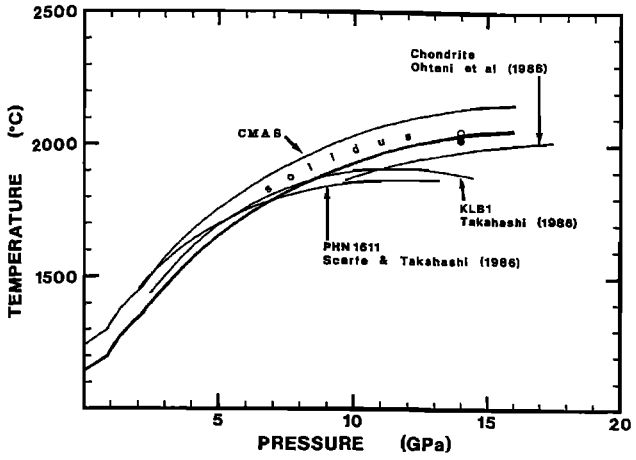

Fig. 21. Experiments on a natural peridotite KLB1 showing brackets on the solidus (KLB1-2 and KLB1-3; see also Figure 3). The solidus in CMAS is from Figure 4 and is about 100° higher than the solidus for KLB1 at 14 GPa. The heavy curve labeled "solidus" is a recommended solidus for natural upper mantle peridotite, based on the observation that components such as FeO tend to lower the solidus in CMAS by about 100°C at all pressures (see text).

technique used by Takahashi and coworkers. Indeed, one of our experiments was similarly affected by water. Two experiments were run at 14 GPa and 2020°C. In one the sample was thoroughly dry (KLB1-2), and in the other it was inadvertently exposed to water in the air on a humid day for about 1 min prior to running (KLB1-1). The truly anhydrous experiment yielded a completely crystalline run product. However, the one exposed to the air showed pervasive melting, in both the hot spot and the cold end of the charge that was exposed to the air. This demonstrates the importance of small amounts of water in affecting melting temperatures.

The second explanation for these discrepancies may lie in the different thermocouple configurations used. We discussed above the fact that side-entering thermocouples, the design used in the Misasa experiments, are likely to yield temperatures that are somewhat too low.

The solidus for KLB1 at 14 Gpa demonstrates that the solidus in CMAS is lowered by 100° because of the effects of other components such as FeO (Figure 21). We note with unique interest that 100° is also the amount by which these other components lower the CMAS solidus in the 1-atm to 2.5-GPa pressure range [*Herzberg*, 1983]. For this reason we offer an interpolated solidus for natural complex mantle rocks in Figure 21, based on a 100° lowering of our precisely determined solidus in CMAS throughout the 5- to 15-GPa range (Figure 4).

The temperature where olivine begins to crystallize in the liquid is within the liquidus bracket, which is between 2115°C and 2155°C. Again, this is about 150°C higher than that reported by *Takahashi* [1986]. Our liquidus temperature at 14 GPa is about 200° lower than the melting temperature of pure forsterite (Figure 11), a freezing point depression that is caused by FeO in addition to CaO and Al_2O_3 (and other trace components to a lesser extent). This compares with a freezing point depression of around 200°C at 1 atm (Figure 11). These results indicate that the olivine liquidus curve for KLB1 is approximately parallel to the fusion curve of forsterite, an observation made also from our CMAS results. The negative slopes to the olivine liquidii for KLB1 and PHN 1611 that appears in the Misasa data at pressures greater than 8 GPa are inconsistent with our results and the fusion curve of forsterite which remains positive at all pressures (Figure 11).

Electron microprobe analyses were determined on coexisting phases, with special attention focused on compositional variations in olivine and garnet along the temperature gradient. Representative analyses are given in Table 5. The ratio Mg/(Mg + Fe) is quite uniform through the charge that contains no melt phase. However, it increases systematically at temperatures above the solidus (Figure 22), demonstrating that Fe partitions preferentially into the melt. Olivine becomes highly magnesian near the liquidus ($Fo_{96.8}$), showing values that are almost identical to those reported by *Takahashi* [1986]. The majorite garnets have a great deal of pyroxene dissolved in them, as is seen by their low alumina and high silica contents (Table 5).

Divalent iron and magnesium are distributed among coexisting phases according to the following exchange reactions:

$$Mg_{Ol} + Fe_{Gt} = Fe_{Ol} + Mg_{Gt} \quad (1)$$

$$Mg_{Ol} + Fe_{Cpx} = Fe_{Ol} + Mg_{Cpx} \quad (2)$$

$$Mg_{Cpx} + Fe_{Gt} = Fe_{Cpx} + Mg_{Gt} \quad (3)$$

$$Mg_{Ol} + Fe_{L} = Fe_{Ol} + Mg_{L} \quad (4)$$

where the distribution coefficients take the form

$$K_D^1 = Fe_{Ol}Mg_{GT}/Mg_{Ol}Fe_{Gt}$$

and so on. For all crystalline phases coexisting at and below the solidus, iron partitions preferentially into garnet. Atomic ratios of Mg/(Mg + Fe) are 0.899, 0.884, and 0.862 for Ol, Cpx, and Gt, respectively (Table 5). On the basis of averages of 10 olivines, 12 garnets, and nine pyroxenes located in the subsolidus, the distribution coefficients are $K_D^1 = 0.72$, $K_D^2 = 0.88$, and $K_D^3 = 0.82$. At temperatures between the liquidus and the solidus where the phase assemblage is L + Ol + Gt, K_D^1 averages 0.71 for eight coexisting olivine-garnet pairs, demonstrating that iron and magnesium partitioning does not change significantly across a temperature range of 100°.

The distribution of iron and magnesium between olivine and liquid is difficult to evaluate because of analytical problems associated with a highly magnesian liquid that quenches to a dense mat of rapidly cooled skeletal olivines, pyroxenes, Fe metal, and other phases too small to identify. Broad-beam techniques are often used [*Ohtani et al.*, 1986], but ambiguities arise when Fe metal droplets are included in the analysis. This is serious because Fe metal is a ubiquitous phase in all iron-bearing experiments, and this demonstrates that the oxygen fugacity in these assemblies is lower than the iron-wustite buffer. Usually, the metal phase is pure Fe when carbon capsules are used [e.g., *Kato and Kumazawa*, 1986; *Ohtani et al.*, 1986], but in our experiments the metal droplets are a Mo-Fe alloy (see above) because of the molybdenum container. The amount of metal we observe is typically about 10–20% of the liquid volume, but in places it reaches up to 50% (see above). The actual amount of iron that has been reduced from FeO is difficult to estimate because the metal droplets are so heterogeneous in composition; however, we estimate that it may be 20–50%.

TABLE 5. Representative Mineral Analyses in KLB1-3

Phase	Ol*	Gt*	Cpx*	Ol†	Gt†	Ol‡	Gt‡	Ol§	Gt§	Ol‖	Gt‖
SiO_2	41.23	49.55	54.38	41.55	52.05	41.82	49.64	42.21	50.91	41.75	50.30
TiO_2	0.01	0.54	0.11	0.00	0.19	0.00	0.13	0.01	0.07	0.03	0.07
Al_2O_3	0.12	9.60	1.50	0.10	8.77	0.14	10.63	0.18	12.10	0.16	12.67
Cr_2O_3	0.00	0.99	0.30	0.08	0.82	0.10	0.76	0.11	0.77	0.17	0.67
FeO	9.89	7.28	5.13	5.59	5.00	3.94	3.63	3.81	2.97	3.19	2.36
MnO	0.11	0.25	0.17	0.14	0.22	0.01	0.10	0.01	0.13	0.00	0.06
MgO	49.29	25.55	21.86	52.51	29.64	54.08	30.89	54.53	31.36	54.46	32.23
CaO	0.30	6.66	14.93	0.27	4.43	0.15	3.46	0.14	2.33	0.10	1.88
Na_2O	0.03	0.22	1.04	0.08	0.13	0.00	0.07	0.00	0.06	0.00	0.06
Total	100.97	100.64	99.42	100.32	101.26	100.23	100.00	100.71	99.29	99.86	100.29
Si	1.000	3.502	1.966	0.996	3.584	0.995	3.461	0.996	3.469	0.994	3.429
Ti	0.000	0.029	0.003	0.000	0.010	0.000	0.007	0.000	0.004	0.000	0.004
Al	0.003	0.800	0.064	0.003	0.712	0.004	0.874	0.005	0.972	0.004	1.018
Cr	0.000	0.055	0.009	0.002	0.045	0.002	0.042	0.002	0.041	0.003	0.036
Fe	0.201	0.430	0.155	0.112	0.288	0.078	0.212	0.075	0.169	0.064	0.135
Mn	0.002	0.015	0.005	0.003	0.013	0.000	0.006	0.000	0.008	0.000	0.003
Mg	1.782	2.692	1.178	1.877	3.042	1.918	3.210	1.918	3.185	1.933	3.275
Ca	0.008	0.504	0.578	0.007	0.327	0.004	0.258	0.004	0.170	0.003	0.137
Na	0.001	0.30	0.073	0.004	0.017	0.000	0.009	0.000	0.008	0.000	0.008
O	4.000	12.000	6.000	4.000	12.000	4.000	12.000	4.000	12.000	4.000	12.000
Mg/(Mg + Fe)	0.899	0.862	0.884	0.944	0.914	0.961	0.938	0.962	0.950	0.968	0.960

*Subsolidus.
†Relative position between solidus (zero) and liquidus (1): 0.25.
‡Relative position between solidus (zero) and liquidus (1): 0.67.
§Relative position between solidus (zero) and liquidus (1): 1.00.
‖Relative position between solidus (zero) and liquidus (1): 1.00.

In principle, the partitioning of iron and magnesium between olivine and liquid is possible without direct analysis of the liquid phase from simple mass balance with the known starting composition of KLB1. That is, K_D^4 can be calculated from olivine analyzed at or near the liquidus where the composition of the liquid should be close to that of the bulk composition of the sample. However, in practice this is not reliable as long as Fe metal is present because the FeO

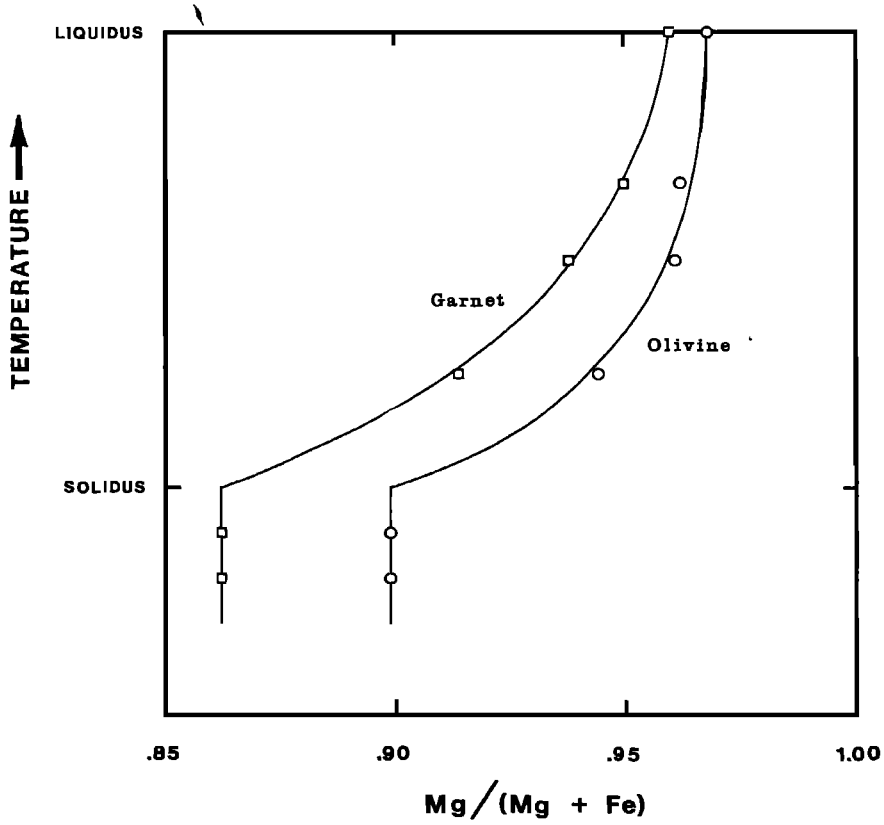

Fig. 22. Changes in the composition of coexisting olivines and garnets in KLB1-3, from data in Table 5.

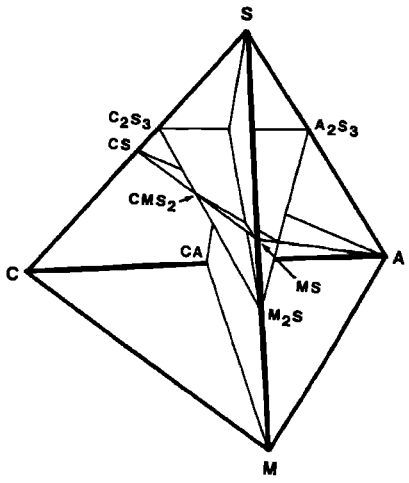

Fig. 23. Three planes and points of projection within the tetrahedron C-M-A-S.

content of the liquid phase becomes unknown. The Mg/(Mg + Fe) for these olivines are too high (Table 5) for the unreduced FeO content of the starting material. For example, if we assume that no FeO has been reduced to Fe metal in our experiments, we determine K_D^4 to be 0.27. This is similar to coexisting olivine and basaltic glasses at 1 atm [*Roedder and Emslie*, 1970]. The logical inference from these data is that pressure has no effect on the partitioning of iron and magnesium between olivine and liquid. But this conclusion would be valid only if FeO was not reduced to Fe metal in these experiments. A loss of 50% FeO to Fe metal would increase K_D^4 from 0.27 to 0.54 at 14 GPa in our experiments. We conclude that all determinations of K_D^4 are likely to remain suspect unless it can be demonstrated that the redox state of iron in the experiment has been carefully controlled.

4. Discussion of Results

The system CaO-MgO-Al_2O_3-SiO_2 is represented in Figure 23, and within this tetrahedron, three planes and three points of projection are orientated. The first of these that we will consider is a projection of rock compositions and experimental data from diopside into the plane CA-M-S, and this is shown in Figure 24. The compositions of liquids produced by partial melting at low pressures are well known and provide a frame of reference for understanding the high-pressure data. They range from basalt at 1 atm to picrite at 2.5 GPa [*O'Hara*, 1968; *Longhi*, 1987; *Presnall et al.*, 1979; *Elthon and Scarfe*, 1984; Stolpher, 1980].

Unlike low-pressure data, the compositions of high-pressure ultrabasic liquids cannot be determined directly because they solidify to a complex mat of quench crystals (see above). However, the isobaric crystallization sequence determined for each composition constrains the location of

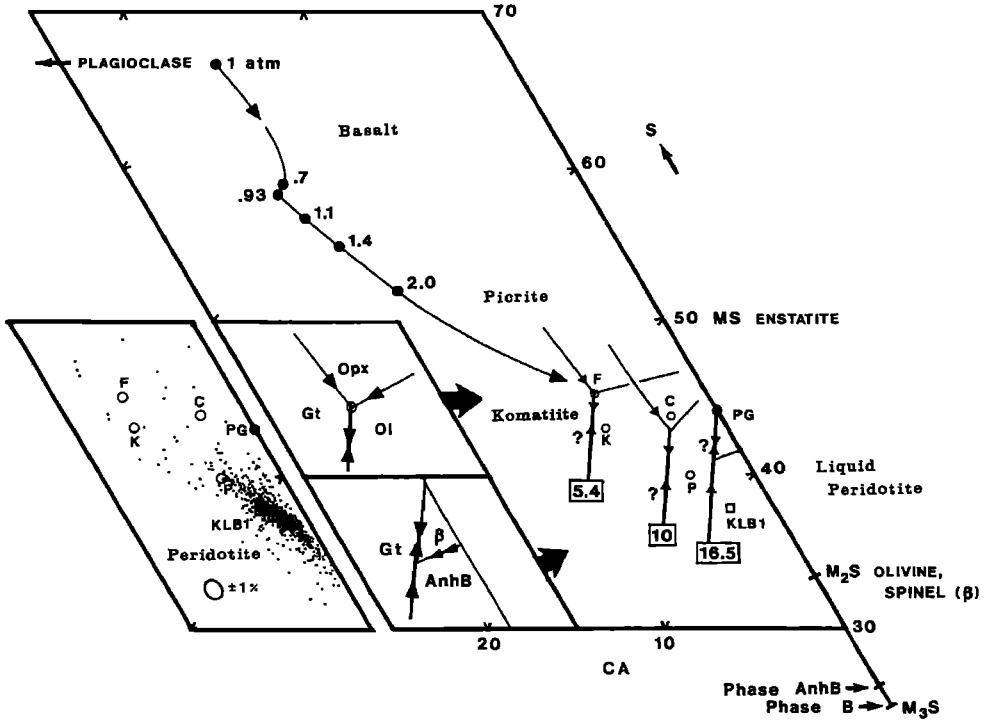

Fig. 24. A projection from diopside (CMS_2) into part of the plane CA-M-S (mole percent projection adapted from *O'Hara* [1968]). Solid circles are the compositions of liquids formed by isobaric invariant melting on the solidus in CaO-MgO-Al_2O_3-SiO_2: 1 atm from *Longhi* [1987] and 0.7–2.0 GPa from *Presnall et al.* [1979]. Experimental compositions K, P, C, and KLB1 are from this study, the komatiite composition F is from *Fujii et al.* [1989], and PG is from *Presnall and Gasparik* [this issue]. At 5.4 and 10 GPa, all crystallization fields and cotectic boundaries are saturated in clinopyroxene in addition to the phases shown. The inset shows a world data base of naturally occurring peridotites from *Herzberg et al.* [1988]. The invariant points L + Gt + Sp and L + Gt + AnhB + Sp at 16.5 GPa have not been rigorously bracketed, but they are bounded to low contents of CA by the extraction of majoritic garnet (Table 4) from the bulk composition.

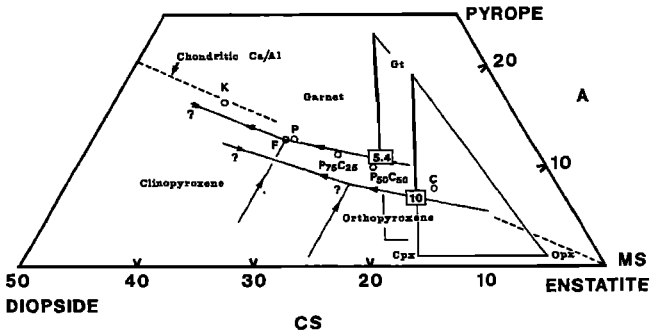

Fig. 25. A projection from olivine (M_2S) into part of the plane CS-MS-A (mole percent [*O'Hara*, 1968]). Garnet, clinopyroxene, and orthopyroxene compositions are those on the solidus at the pressures indicated. Data at 10 GPa are from Table 4. Compositions at 5.4 GPa are estimated from *Carlson and Lindsley* [1988] and *Gasparik* [1984]. All crystallization fields and cotectic boundaries are saturated in olivine, in addition to the phases shown.

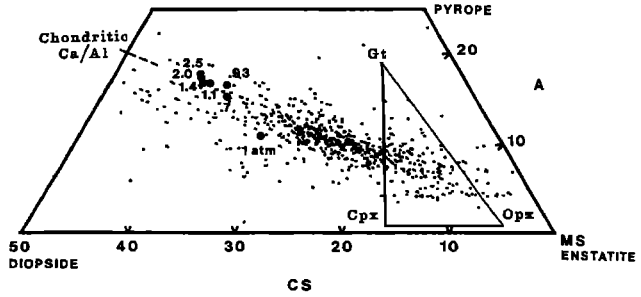

Fig. 26. A world data base of mantle peridotites [*Herzberg et al.*, 1988] projected from olivine into the plane CS-MS-A. The invariant peritectic points are those in Figure 24. Garnet, clinopyroxene, and orthopyroxene compositions are those on the solidus at 10 GPa (Figure 25), demonstrating that most peridotites must crystallize to an orthopyroxene-free assemblage of Ol + Cpx + Gt.

the various isobaric invariant points of interest. The first is for the equilibrium L + Ol + Opx + Cpx + Gt. All five phases were reported by *Fujii et al.* [1989] to occur along an isotherm in their experiment at 5.4 GPa. This is very fortunate because it means that the bulk composition (F; Figure 24) is similar to the composition of the liquid phase (L) at this invariant point. It has 32.2% MgO, a komatiite analogue in CMAS.

Before experimental data in this high-pressure region were available, various theoretical arguments led to the conclusion that the isobaric invariant point at around 5 GPa could be eutectic [*Irvine and Sharpe*, 1982; *Herzberg and O'Hara*, 1985]. This, however, is not the case. Reference to Figure 25 demonstrates that it is peritectic instead. The composition of the liquid (L) lies outside all compositions bounded by Ol + Opx + Cpx + Gt at around 5 GPa, largely because the clinopyroxene is compositionally more akin to enstatite than it is to diopside. The phases L and Opx are located on opposite sides of the plane Ol + Cpx + Gt, requiring the peritectic to be L + Opx = Ol + Cpx + Gt. Removal of heat would drive the liquid to a cotectic involving L + Ol + Cpx + Gt, producing residual liquids with lower silica contents. We provide evidence below, however, which shows that these liquids do not become highly undersaturated because the cotectic is likely to degenerate into a thermal minimum near the invariant point itself.

Our experimental data on komatiite (K) show that the sample is multiply saturated in olivine and garnet at 6.3 GPa. However, none of our experiments contain orthopyroxene because the bulk composition has a lower enstatite content (Figure 24). Apart from this difference, there is good agreement between the two sets of data. Figure 24 shows that the effect of pressure is to expand the stability field of garnet from compositions like F to K over an interval of about 1 GPa.

Upper mantle peridotites and their analogues (P and KLB1) crystallize to the three-phase assemblage Ol + Cpx + Gt over a wide pressure range. Orthopyroxene is usually absent, mainly because of the extensive solubility of enstatite in clinopyroxene (Figures 25 and 26), but it can appear at temperatures above the solidus (P-07).

Orthopyroxene is an important crystallizing phase for compositions that are enriched in enstatite compared to upper mantle peridotite ($P_{50}C_{50}$ and C; Figure 25). The isobaric peritectic point L + Opx = Ol + Cpx + Gt is constrained to shift to liquid compositions that are highly magnesian, from komatiite at 5 GPa to peridotitic compositions having around 40% MgO. Although ultrabasic, they are unlike mantle peridotite in that they are distinctly enriched in silica (Figure 24). A critical question thus emerges. Is there a link between liquids formed at these invariant points and mantle peridotite? A link is certainly anticipated because silica-enriched liquids formed by invariant melting are forced to become similar to mantle peridotite with the removal of orthopyroxene and fractionation along the cotectic L + Ol + Cpx + Gt. However, it is not yet clear if mantle peridotite can form in this way because a range of possible silica contents exist along the cotectic, and these have yet to be calibrated by experiment. At one extreme is the possibility that very low silica contents could be formed, values that are lower than and unlike those observed for mantle peridotite. A much more interesting possibility is one where the cotectic L + Ol + Cpx + Gt degenerates into a thermal minimum L + Ol + Cpx + Gt with L compositionally identical to mantle peridotite. This is particularly important because, if shown to be correct, it would support that class of model which connects the major element geochemistry of mantle peridotite to high-pressure invariant points such as eutectics [*Herzberg and O'Hara*, 1985] and thermal minima. A third possibility is similar to the second, except the composition of the liquid at the thermal minimum is enriched in silica compared to mantle peridotite, similar in composition to the peritectic point itself. Clearly, there is a pressing need to test these possibilities.

There are several lines of evidence that point to the stability of a thermal minimum L + Ol + Cpx + Gt, and one that is not highly deficient in silica. Part of this evidence stems from experimental data at 16.5 GPa. Our experiment on chondrite at this pressure shows the isobaric crystallization sequence to be L, L + Gt, L + Gt + AnhB, L + Gt + Sp, and Gt + Sp. Other pertinent observations are that modified spinel melts incongruently to phase AnhB + L (silica-rich), that pyroxenes are not stable [*Gasparik*, 1989], and that the garnets are majoritic. The cotectic equilibrium involving L + Gt + AnhB must yield silica-enriched liquids with the extraction of heat (Figure 24). At somewhat lower pressures, three important changes occur: phase AnhB becomes unstable; modified spinel reverts to olivine; and

clinopyroxene becomes stable. This will probably occur at around 15 GPa, and when it does occur, the cotectic equilibrium involving AnhB must transform to L + Ol + Cpx + Gt. There is a definite limit to silica undersaturation seen at 16.5 GPa, one that probably exists at lower pressures as well. This is consistent with the experimental work of *Presnall and Gasparik* [this issue] on the join enstatite-forsterite which shows little shift in the 16.5-GPa eutectic (Figure 24) to more Mg-rich compositions at higher pressures.

There exists another piece of evidence pointing to the stability of a thermal minimum L + Ol + Cpx + Gt. The solidus temperatures for chondrite are very similar to those for peridotite, although an exact determination was not made. Furthermore, the solidus temperature for komatiite at 11.6 GPa (K-10) also appears to be very similar to that for mantle peridotite (P-02). This is circumstantial evidence indicating that the liquid composition at the thermal minimum may not be all that different from the liquid composition at the peritectic. Indeed, we expect it to be contained within the compositional space defined by the end-members olivine-diopside-enstatite-pyrope; the reason it is a thermal minimum instead of a eutectic as suggested by *Irvine and Sharpe* [1982], *Herzberg* [1983], and *Herzberg and O'Hara* [1985] is because the large amount of enstatite dissolved in clinopyroxene forces a contraction to occur in the compositional space occupied by Ol-Cpx-Opx-Gt, and the liquid is left outside it.

Although a large gap remains in the experimental data base, the information discussed above permits an evaluation to be made of current melting and crystallization models for the origin of the upper mantle. Figure 24 demonstrates that initial melting of a chondritic mantle composition would yield a peridotite liquid, but one that is higher in silica than typical mantle peridotite. Therefore the upper mantle could not have formed from the solidification of these liquids as proposed by *Herzberg and O'Hara* [1985]. If it can be confirmed by experiment that there is a coincidence in the composition of mantle peridotite and a thermal minimum, it would be a strong endorsement of an upper mantle that formed by fractional crystallization, rather than by fractional melting.

The projection of mantle peridotites in the plane CS-MS-A yields a trend defined by variations in enstatite, and this is shown in Figure 26. This trend, however, is largely an illusion, because geochemical variations in mantle peridotite are described mainly by variations in olivine content, as is illustrated in Figure 24. The more magnesian members of this trend (i.e., about 47% MgO) are often considered residues, whereas those with the lowest MgO contents (36% MgO) are considered fertile or primitive upper mantle. There is, however, a minor but important contribution from enstatite which gives rise to the trend in Figure 26. This can be visualized by examining simultaneously the peridotite compositions in Figures 24 and 26. The peridotite "trend" shown in Figure 24 is not actually an "olivine control," in that it cannot be a mixture of olivine and some other component such as komatiite. Its extrapolation to the M-S join is located between olivine and enstatite, not to olivine. This departure from an olivine control trend becomes greatly distorted and magnified by projection from olivine (Figure 26). The utility of the projection is that it unambiguously disproves that class of model which explains the major element geochemistry of mantle peridotite as a two-component mixture of olivine and basalt [*Ringwood*, 1962] or olivine and a komatiitelike liquid [*Agee and Walker*, 1988].

In addition to being highly magnesian, mantle peridotites are characteristically nonchondritic in terms of CaO/Al_2O_3. The lime and alumina contents for our world data base of peridotites are summarized in Figure 27. These are raw data that have been compiled uncritically, and there are 668 analyses in the data base. The rocks consist mainly of spinel peridotites from all locations in the world but include garnet peridotites in addition to harzburgites from ophiolite complexes. The only samples omitted are those from South Africa. These are largely the coarse-grained and low-temperature peridotite xenoliths from kimberlite. They differ from the more "typical" mantle peridotites from the world in almost every geochemical parameter, including lime to alumina [*Boyd and Mertzman*, 1987; *Herzberg et al.*, 1988], and they are confined to the continental lithosphere in South Africa [*Boyd*, 1987]. In contrast, the more typical spinel-type peridotites that make up our mantle data base originate in the asthenosphere or the oceanic lithosphere. The important point is that $CaO/(CaO + Al_2O_3)$ for samples of typical mantle peridotite is usually greater than chondritic (Figure 27), a point emphasized previously by *Palme and Nickel* [1985]. The weight percent averages for 668 analyses in Figure 28 are CaO = 2.43 wt %, Al_2O_3 = 2.53 wt %, and $CaO/(CaO + Al_2O_3) = 0.49$, in good agreement with averages given by *Maaloe and Aoki* [1977]. These differ from pyrolite [*Ringwood*, 1979] and chondrite, both of which have $CaO/(CaO + Al_2O_3) = 0.44$. The upper mantle is definitely not chondritic in these elements.

We now examine how lime/alumina in mantle peridotite compares to high-pressure liquids that are located at peritectic points and thermal minima, and this can be seen by comparing Figures 25 and 26. At around 5 GPa the liquid composition in L + Opx = Ol + Cpx + Gt is well constrained [*Fujii et al.*, 1989]. It is komatiitic with lime/alumina that is also higher than chondrite, essentially identical to mantle peridotite. At even higher pressures the primary crystallization field of garnet is observed to expand at the expense of clinopyroxene, but by an amount that has not been bracketed by experiment. This is consistent with the well-documented expansion of the stability of garnet at the expense of pyroxenes at temperatures below the melting point [*Akaogi and Akimoto*, 1977; *Liu*, 1977; *Kanzaki*, 1987; *Gasparik*, 1989].

A simpler way of depicting relations among lime and alumina is shown in an alternative projection (Figure 28). The plane of projection contains the phases olivine, pyrope, and diopside, and the compositions of naturally occurring mantle peridotite lie almost in it, but to the silica-rich side. This projection is particularly useful because the wide range of normative olivine contents seen in Figure 24 is reproduced faithfully, and it shows lime and alumina contents as well. The point of projection is enstatite, and the peritectic equilibrium L + Opx = Cpx + Gt + Ol appears as a eutectic (Figure 28). The cotectic and thermal minimum involving L + Cpx + Gt + Ol should project close to the peritectic, rendering Figure 28 applicable to all melting and crystallization possibilities. Uncertainties in the silica content of the thermal minimum L + Ol + Cpx + Gt (Figure 24) are essentially suppressed by projection from enstatite.

All experimental work shows an expansion in the stability

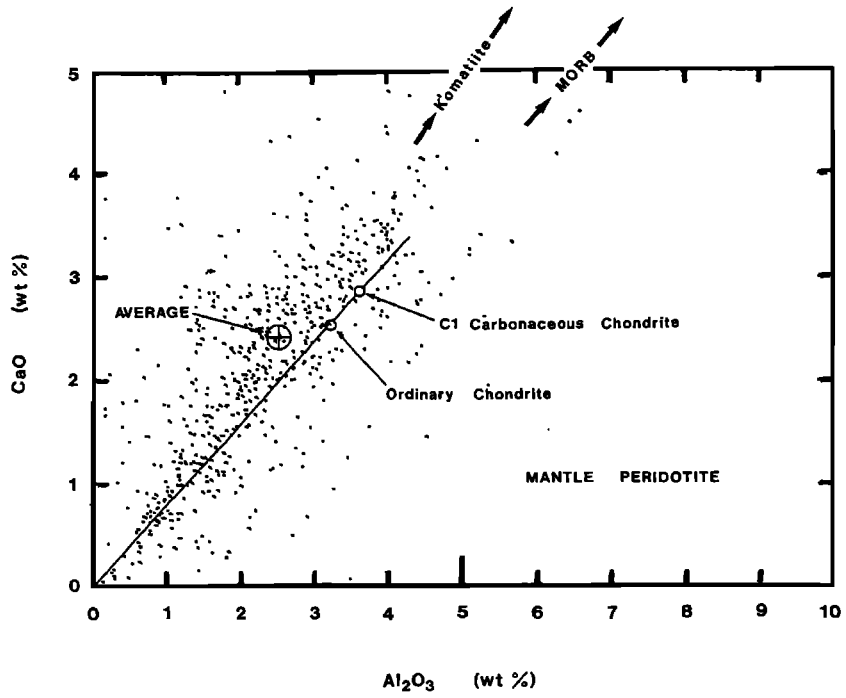

Fig. 27. Lime and alumina contents of mantle peridotites (weight percent) from the world data base reported by *Herzberg et al.* [1988] and their average. Chondritic values are from *Anders and Ebihara* [1982] (C1, carbonaceous) and *Dodd* [1981] (ordinary), calculated metal-free and with Mg/(Mg + Fe) = 0.90 (molar).

field of liquidus garnet with increasing pressure (Figure 28). Where clinopyroxene occurs, it is invariably on the solidus. This requires that lime/alumina for liquids in L + Ol + Cpx + Gt increase with pressure from 5 GPa to the 10- to 15-GPa range. The amount shown in Figure 28 has not been bracketed by experiment. To do so would require the observation of liquidus clinopyroxene in appropriate compositions. However, the important observation to be made is that lime/alumina is distinctly higher than chondritic for both mantle peridotite occurring naturally and liquids at high-pressure invariant points. Indeed, *Fujii et al.* [1989] suggested that $CaO/(CaO + Al_2O_3)$ could shift from around 0.49 at 5 GPa to around 0.60 at higher pressures, values that are more characteristic of komatiites from Barberton. If this is correct, partial melting of normal mantle peridotite at high pressures could then explain these high ratios [*Fujii et al.*, 1989]. This would be a plausible alternative to the suggestion that the source region of the Barberton komatiites was atypically high in lime to alumina [*Cawthorn and Strong*, 1974; *Herzberg and Ohtani*, 1988; *Anderson*, 1989].

The observation of liquidus clinopyroxene is critical in constraining further the compositions of high-pressure liq-

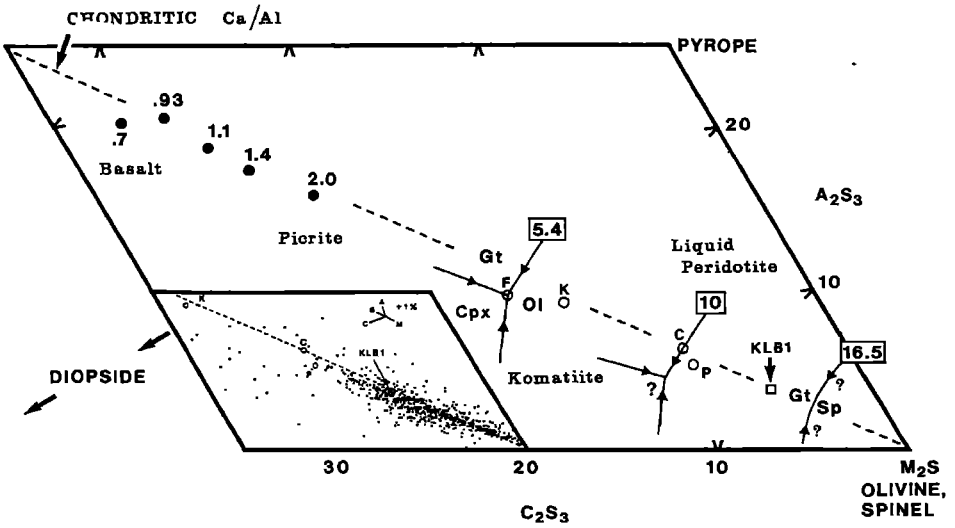

Fig. 28. A projection to and from enstatite (MS) into part of the plane M_2S-C_2S_3-A_2S_3 (mole percent *O'Hara*, 1968]). Mantle peridotites are shown in the inset. At 5.4 and 10 GPa all crystallization fields and cotectic boundaries are saturated in orthopyroxene in addition to the phases shown.

uids multiply saturated in olivine, clinopyroxene, and garnet. Its correct identification can be a nontrivial experimental problem because it can appear similar to quench clinopyroxenes. Indeed, readers should note that the phase diagrams reported by one of us [*Herzberg and Ohtani*, 1988] are now obsolete because quench clinopyroxene was erroneously identified as being primary (see Figure 9). However, liquidus clinopyroxene has been reported by *Wei et al.* [this issue] on a natural komatiite from the Barberton Mountain Land. We have purposefully omitted experimental data from natural compositions because the preferential partitioning of Fe in garnet (Figure 22) will expand its stability field and increase lime/alumina in liquids even more. Although this information is clearly more relevant to the Earth than experimental data in simplified analogue systems, an important ambiguity emerges. FeO contents for natural komatiites are typically 10–13%, higher than for mid-ocean ridge basalts (MORB) and mantle peridotite. The field observation of widespread olivine cumulates associated with these komatiite flows indicates that the high FeO contents arise from olivine fraction; primary komatiitic magmas that formed at depth were likely to have had much lower contents of FeO.

The lime and alumina contents for mantle peridotite define a trend in Figure 27, although it is obvious that considerable scatter exists. A linear regression yields $CaO = 1.03(Al_2O_3) - 0.18$ (weight percent). Komatiites from most locations in the world except Barberton plot exactly on this trend and have $CaO/(CaO + Al_2O_3) = 0.49$ by weight. This is distinctly higher than normal MORB or primitive MORB glasses (0.43 [*Presnall and Hoover*, 1987; *Melson et al.*, 1976]). Consequently, the removal of basalt (0.43) from fertile mantle peridotite (0.49) would produce complementary refractory peridotites and harzburgites with compositions greater than 0.50. Although these high ratios do exist as scatter to the trend, they are not characteristic of normal mantle peridotite. Similarly, model mantle compositions based on the addition of basalt to refractory peridotite (e.g., pyrolite [*Ringwood*, 1979]) fail to explain these lime and alumina abundances. The implication is that many peridotites developed refractory lime and alumina abundances because of komatiite extraction in the Archean and that basaltic crust formation in comparatively recent times has not erased the geochemical record of this ancient event.

The most straightforward way of interpreting komatiites that have lime/alumina ratios that are identical to mantle peridotite is by high degrees of partial melting of a peridotite source. The MgO content of komatiites, however, is not a good indicator of the degree of partial melting [*Herzberg and Ohtani*, 1988], and the experimental data of *Fujii et al.* [1989] and *Wei et al.* [this issue] confirm that komatiites could have formed by moderate degrees of invariant melting. Archean analogues of present-day mantle plumes could have been deeper and more energetic, with extensive melting in the core and low degrees of partial melting at the periphery [*Herzberg and Ohtani*, 1988]. If this occurred at high pressures, the different possibilities may not be obvious in the major element geochemistry of komatiites. From a phase equilibrium point of view, these questions cannot be properly addressed at the present time because the partial melting products of peridotite differ from those of chondrite. Unlike chondrite, partial melting of mantle peridotite does not usually involve orthopyroxene, generating instead liquids somewhere along a cotectic L + Ol + Cpx + Gt. These liquids will have compositions that are similar to one uniquely defined by an isobaric thermal minimum. Initial melting cannot be strictly invariant, except if it occurs at the thermal minimum, and this will result in a liquid composition that can vary to a certain extent with the composition of the peridotite being melted, even in a four-component analogue system. In general, however, these initial melts have close compositional affinities to komatiite at 5 GPa and mantle peridotite at 10–15 GPa (Figure 28).

5. CONCLUSIONS

Experimental work on analogue komatiite, peridotite, and chondrite compositions has permitted an exploration to be made of melting and crystallization phenomena in the range 5–16.5 GPa. The melting of rocks which contain the four crystalline phases olivine, orthopyroxene, clinopyroxene, and garnet is restricted to enstatite-rich compositions such as chondrite. For these compositions it is demonstrated that melting is peritectic, rather than eutectic, and it takes the form L + Opx = Ol + Cpx + Gt. Partial melting generates liquids with the following characteristics: 5 GPa for komatiite and 10–15 GPa for liquid peridotite with about 40% MgO, but one that is unlike mantle peridotite in that it is distinctly enriched in silica. It is demonstrated, therefore, that upper mantle peridotite could not have originated by direct initial melting of a chondritic mantle, a refutation of the partial-melting model of *Herzberg and O'Hara* [1985].

Unlike chondrite, partial melting of mantle peridotite at high pressures does not usually involve orthopyroxene. Instead, it occurs by the generation of ultrabasic liquids along a cotectic involving L + Ol + Cpx + Gt. Although the thermal and compositional characteristics of this cotectic have not been fully calibrated, it will degenerate into a thermal minimum (L + Ol + Cpx + Gt), compositionally similar to komatiite at 5 GPa and mantle peridotite at 10–15 GPa.

Peridotite liquids that occupy a thermal minimum can be derived from those formed from the melting of chondrite by removal of orthopyroxene, followed by fractional crystallization of olivine, clinopyroxene, and garnet. The possibility exists that the thermal minimum is compositionally identical to upper mantle peridotite in the 10- 15-GPa range. If this can be confirmed by experiment, it would support the hypothesis of an upper mantle that originated by fractional crystallization of peridotite liquids in a large-scale crystallization-differentiation event. In the absence of additional experimental data a detailed exploration of the different ways that this could have occurred is somewhat premature. However, it is worth noting that all plausible explanations for the occupation of mantle peridotite in a thermal minimum would probably have to involve fractional crystallization at great depths, consistent with magma ocean models.

Acknowledgments. This paper is dedicated to the memory of Chris Scarfe, who was my good friend (C.H.) Many individuals contributed to this paper. In particular, we would like to thank Robert Hutchison, Sven Maaloe, Mineo Kumazawa, Takumi Kato, Keish Hasebe, Eiji Ohtani, Roger Hewins, Jeremy Delaney, Mike Carr, Mark Feigenson, Kejian Wei, Bob Liebermann, Don Weidner, Mike O'Hara, and Dean Presnall. Special thanks go to Reidar Tronnes and Eiichi Takahashi for their thorough and perceptive reviews. This research was supported by grants from the National Science Foundation to C.H. (INT 84-18484) and T.G. (EAR 86-

17550). The high-pressure facilities at Stony Brook were made possible by support from NSF (EAR 86-07105) and the State University of New York at Stony Brook.

REFERENCES

Agee, C. B., and D. Walker, Mass balance and phase density constraints on early differentiation of chondritic mantle, *Earth Planet. Sci. Lett.*, *90*, 144–156, 1988.

Akaogi, M., and S. Akimoto, Pyroxene-garnet solid-solution equilibria in the systems $Mg_4Si_4O_{12}$-$Mg_3Al_2Si_3O_{12}$ and $Fe_4Si_4O_{12}$-$Fe_3Al_2Si_3O_{12}$ at high pressures and temperatures, *Phys. Earth Planet. Inter.*, *15*, 90–106, 1977.

Anders, E., and M. Ebihara, Solar-system abundances of the elements, *Geochim. Cosmochim. Acta*, *46*, 2363–2380, 1982.

Anderson, D. L., Composition of the Earth, *Science*, *243*, 367–370, 1989.

Boyd, F. R., High- and low-temperature garnet peridotite xenoliths and their possible relation to the lithosphere-asthenosphere boundary beneath southern Africa, in *Mantle Xenoliths*, edited by P. H. Nixon, pp. 403–412, John Wiley, New York, 1987.

Boyd, F. R., and S. A. Mertzman, Composition and structure of the Kaapvaal lithosphere, southern Africa, Magmatic Processes: Physicochemical Principles, edited by B. O. Mysen, *Geochem. Soc. Spec. Publ. 1*, pp. 13–24, Lancaster Press, Lancaster, 1987.

Carlson, W. D., and D. H. Lindsley, Thermochemistry of pyroxenes on the join $Mg_2Si_2O_6$-$CaMgSi_2O_6$, *Am. Mineral.*, *73*, 242–252, 1988.

Cawthorn, R. G., and D. F. Strong, The petrogenesis of komatiites and related rocks as evidence for a layered upper mantle, *Earth Planet. Sci. Lett.*, *23*, 369–375, 1974.

Davis, B. T. C., and J. F. Schairer, Melting relations in the join diopside-forsterite-pyrope at 40 kilobars and at one atmosphere, *Year Book Carnegie Inst. Washington*, *64*, 123–126, 1965.

Dodd, R. T., *Meteorites*, 368 pp., Cambridge University Press, New York, 1981.

Elthon, D., and C. M. Scarfe, High-pressure phase equilibria of a high-magnesia basalt and the genesis of primary oceanic basalts, *Am. Mineral.*, *69*, 1–15, 1984.

Feigenson, M. D., and M. J. Carr, Determination of major, trace and rare-earth elements in rocks by DCP-AES, *Chem. Geol.*, *51*, 19–27, 1985.

Finger, L. W., J. Ko, R. M. Hazen, T. Gasparik, R. J. Hemley, C. T. Prewitt, and D. J. Weidner, Crystal chemistry of phase B and an anhydrous analogue: Implications for water storage in the upper mantle, *Nature*, *341*, 140–142, 1989.

Fujii, T., and C. M. Scarfe, Compositions of liquids coexisting with spinel lherzolite at 10 kbar and the genesis of MORBs, *Contrib. Mineral. Petrol.*, *90*, 18–28, 1985.

Fujii, T., M. Tachikara, and K. Kurita, Melting experiments in the system CaO-MgO-Al_2O_3-SiO_2 to 8 GPa: Constraints to the origin of komatiites, *Eos Trans. AGU*, *70*, 483, 1989.

Gasparik, T., Two-pyroxene thermobarometry with new experimental data in the system CaO-MgO-Al_2O_3-SiO_2, *Contrib. Mineral. Petrol.*, *87*, 87–97, 1984.

Gasparik, T., Transformation of enstatite-diopside-jadeite pyroxenes to garnet, *Contrib. Mineral. Petrol.*, *102*, 389–405, 1989.

Gasparik, T., Phase relations in the transition zone, *J. Geophys. Res.*, this issue.

Getting, I. C., and G. C. Kennedy, Effect of pressure on the emf of chromel-alumel and platinum-platinum 10% rhodium thermocouples, *J. Appl. Phys.*, *41*, 4552–4562, 1970.

Green, D. H., W. O. Hibberson, and L. Jaques, Petrogenesis of mid-ocean ridge basalts, in *The Earth: Its Origin, Structure and Evolution*, edited by M. W. McElhinny, pp. 265–299, Academic, San Diego, Calif., 1979.

Hatch, D. M., and S. Ghose, Symmetry analysis of the phase transition and twinning in $MgSiO_3$ garnet: Implications to mantle mineralogy, *Am. Mineral.*, *74*, 1221–1224, 1989.

Herzberg, C. T., The solubility of olivine in basaltic liquids: An ionic model, *Geochim. Cosmochim. Acta*, *43*, 1241–1251, 1979.

Herzberg, C. T., Solidus and liquidus temperatures and mineralogies for anhydrous garnet-lherzolite to 15 GPa, *Phys. Earth Planet. Inter.*, *32*, 193–202, 1983.

Herzberg, C. T., and T. Gasparik, Melting experiments on chondrite at high pressures: Stability of anhydrous phase B, *Eos Trans. AGU*, *70*, 484, 1989.

Herzberg, C. T., and M. J. O'Hara, Origin of mantle peridotite and komatiite by partial melting, *Geophys. Res. Lett.*, *12*, 541–544, 1985.

Herzberg, C. T., and E. Ohtani, Origin of komatiite at high pressures, *Earth Planet. Sci. Lett.*, *88*, 321–329, 1988.

Herzberg, C. T., M. Feigenson, C. Skuba, and E. Ohtani, Majorite fractionation recorded in the geochemistry of peridotites from South Africa, *Nature*, *332*, 823–826, 1988.

Irvine, T. N., and M. R. Sharpe, Source-rock compositions and depths of origin of Bushveld and Stillwater magmas, *Year Book Carnegie Inst. Washington*, *81*, 294–303, 1982.

Ito, E., and E. Takahashi, Melting of peridotite under the lower mantle condition, *Nature*, *328*, 514–517, 1987.

Ito, E., and H. Yamada, Stability relations of silicate spinels, ilmenites and perovskites, in *High-Pressure Research in Geophysics*, edited by S. Akimoto and M. H. Manghnani, pp. 405–419, D. Reidel, Hingham, Mass., 1982.

Kanzaki, M., Ultrahigh-pressure phase relations in the system, $Mg_4Si_4O_{12}$-$Mg_3Al_2Si_3O_{12}$, *Phys. Earth Planet. Inter.*, *49*, 168–175, 1987.

Kato, T., and M. Kumazawa, Effect of high pressure on the melting relation in the system Mg_2SiO_4-$MgSiO_3$, 1, Eutectic relation up to 7 GPa, *J. Phys. Earth*, *33*, 513–524, 1985*a*.

Kato, T., and M. Kumazawa, Garnet phase of $MgSiO_3$ filling the pyroxene-ilmenite gap at very high temperature, *Nature*, *316*, 803–805, 1985*b*.

Kato, T., and M. Kumazawa, Melting experiment on natural lherzolite at 20 GPa: Formation of phase B coexisting with garnet, *Geophys. Res. Lett.*, *13*, 181–184, 1986.

Kato, T., A. E. Ringwood, and T. Irifune, Experimental determination of element partitioning between silicate perovskites, garnets and liquids: Constraints on early differentiation of the mantle, *Earth Planet. Sci. Lett.*, *89*, 123–145, 1988*a*.

Kato, T., A. E. Ringwood, and T. Irifune, Constraints on element partition coefficients between $MgSiO_3$ perovskite and liquid determined by direct measurements, *Earth Planet. Sci. Lett.*, *90*, 65–68, 1988*b*.

Kushiro, I., Origin of some magmas in oceanic and circumoceanic regions, *Tectonophysics*, *17*, 211–222, 1973.

Lesher, C. E., and D. Walker, Cumulate maturation and melt migration in a temperature gradient, *J. Geophys. Res.*, *93*, 10,295–10,311, 1988.

Liu, L, The system enstatite-pyrope at high pressures and temperatures and the mineralogy of the Earth's mantle, *Earth Planet. Sci. Lett.*, *36*, 237–245, 1977.

Longhi, J., Liquidus equilibria and solid solution in the system $CaAl_2Si_2O_8$-Mg_2SiO_4-$CaSiO_3$-SiO_2 at low pressure, *Am. J. Sci.*, *287*, 265–331, 1987.

Maaloe, S., and K. Aoki, The major element composition of the upper mantle estimated from the composition of lherzolites, *Contrib. Mineral. Petrol.*, *63*, 161–173, 1977.

Melson, W. G., T. L. Valier, T. L. Wright, G. Byerly, and J. Nelen, J., Chemical diversity of abyssal volcanic glass erupted along Pacific, Atlantic, and Indian Ocean sea-floor spreading centers, in *The Geophysics of the Pacific Ocean Basin and Its Margin*, *Geophys. Monogr. Ser.*, vol. 19, edited by G. H. Sutton, M. H. Manghnani, and R. Moberly, pp. 351–367, AGU, Washington, D. C., 1976.

O'Hara, M. J., The bearing of phase equilibria studies in synthetic and natural systems on the origin and evolution of basic and ultrabasic rocks, *Earth Sci. Rev.*, *4*, 69–113, 1968.

O'Hara, M. J., M. J. Saunders, and E. L. P. Mercy, Garnet-peridotite, primary ultrabasic magma and eclogite: Interpretation of upper mantle processes in kimberlite, *Phys. Chem. Earth*, *9*, 571–604, 1975.

Ohtani, E., Melting relation of Fe_2SiO_4 up to about 200 kilobars, *J. Phys. Earth*, *27*, 189–208, 1979.

Ohtani, E., and M. Kumazawa, Melting of forsterite Mg_2SiO_4 up to 15 GPa, *Phys. Earth Planet. Inter.*, *27*, 32–38, 1981.

Ohtani, E., and H. Sawamoto, Melting experiment on a model chondritic mantle composition at 25 GPa, *Geophys. Res. Lett.*, *14*, 733–736, 1987.

Ohtani, E., T. Kato, and H. Sawamoto, Melting of a model chondritic mantle to 20 GPa, *Nature*, *322*, 352–353, 1986.

Ohtani, E., T. Irifune, W. O. Hibberson, and A. E. Ringwood, Modified split-sphere guide-block for practical operation of a

multiple-anvil apparatus, *High Temp. High Pressures*, in press, 1990.

Palme, H., and K. G. Nickel, Ca/Al ratio and composition of the Earth's upper mantle, *Geochim. Cosmochim. Acta*, *49*, 2123–2132, 1985.

Presnall, D. C., and T. Gasparik, Melting of enstatite from 10 to 16.5 GPa and the forsterite (Mg_2SiO_4)–majorite ($MgSiO_3$) eutectic at 16.5 GPa: Implications for the origin of the mantle, *J. Geophys. Res.*, this issue.

Presnall, D. C., and J. D. Hoover, High pressure phase equilibrium constraints on the origin of mid-ocean ridge basalts, Magmatic Processes: Physicochemical Principles, edited by B. O. Mysen, *Geochem. Soc. Spec. Publ. 1*, pp. 75–89, Lancaster Press, Lancaster, 1987.

Presnall, D. C., J. R. Dixon, T. H. O'Donnell, and S. A. Dixon, Generation of mid-ocean ridge tholeiites, *J. Petrol.*, *20*, 3–35, 1979.

Ringwood, A. E., A model for the upper mantle, *J. Geophys. Res.*, *67*, 857–866, 1962.

Ringwood, A. E., *Origin of the Earth and Moon*, 295 pp., Springer-Verlag, New York, 1979.

Roeder, P. L., and R. F. Emslie, Olivine-liquid equilibrium, *Contrib. Mineral. Petrol.*, *29*, 275–289, 1970.

Sawamoto, H., Phase diagram of $MgSiO_3$ at pressures up to 24 GPa and temperatures up to 2200°C: Phase stability and properties of tetragonal garnet, in *High-Pressure Research in Mineral Physics*, edited by M. H. Manghnani and Y. Syono, pp. 209–219, Terrapublications, Tokyo, 1987.

Scarfe, C. M., and E. Takahashi, Melting of garnet peridotite to 13 GPa and the early history of the upper mantle, *Nature*, *322*, 354–356, 1986.

Stolper, E., A phase diagram for mid-ocean ridge basalts: Preliminary results and implications for petrogenesis, *Contrib. Mineral. Petrol.*, *74*, 13–27, 1980.

Takahashi, E., Melting of a dry peridotite KLB-1 up to 14 GPa: Implications on the origin of peridotitic upper mantle, *J. Geophys. Res.*, *91*, 9367–9382, 1986.

Takahashi, E., and C. M. Scarfe, Melting of peridotite to 14 GPa and the genesis of komatiite, *Nature*, *315*, 566–568, 1985.

Takahashi, E., H. Yamada, and E. Ito, An ultrahigh-pressure furnace assembly to 100 kbar and 1500°C with minimum temperature uncertainty, *Geophys. Res. Lett.*, *9*, 805–807, 1982.

Walker, D., and S. E. DeLong, Soret separation of mid-ocean ridge basalt magma, *Contrib. Mineral. Petrol.*, *79*, 231–240, 1982.

Wei, K., R. Trønnes, and C. M. Scarfe, Phase relations of aluminum-undepleted and aluminum-depleted komatiites of 4–12 GPa, *J. Geophys. Res.*, this issue.

T. Gasparik, Mineral Physics Institute, Department of Earth and Space Sciences, State University of New York, Stony Brook, NY 11794.

C. Herzberg, Department of Geological Sciences, Rutgers University, New Brunswick, NJ 089030.

H. Sawamoto, Department of Earth Sciences, Nagoya University, Chikusa, Nagoya 464, Japan.

(Received June 30, 1989;
revised December 21, 1989;
accepted January 3, 1990.)